Cell

Resource

A mouse DRG genetic toolkit reveals morphological and physiological diversity of somatosensory neuron subtypes

Graphical abstract

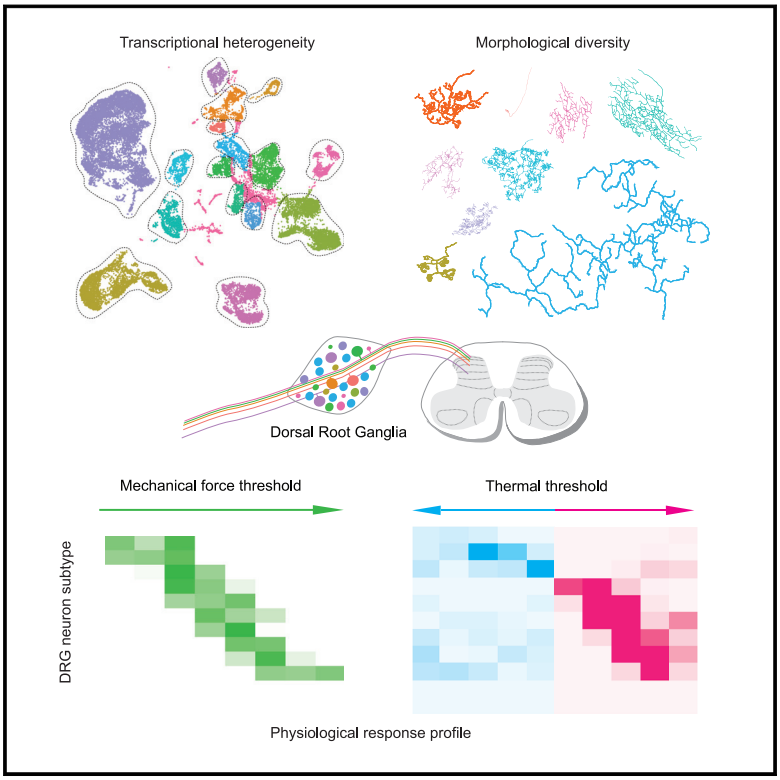

Authors

Lijun Qi, Michael Iskols, David Shi, ..., Isaac M. Chiu, David D. Ginty, Nikhil Sharma

Correspondence

david_ginty@hms.harvard.edu (D.D.G.), ns2151@cumc.columbia.edu (N.S.)

In brief

A DRG neuron genetic toolkit reveals morphological and physiological heterogeneity across the transcriptionally distinct somatosensory neuron subtypes, and findings suggest population coding schemes for the neuronal representation of mechanical and thermal stimuli acting on the skin.

Highlights

- A mouse genetic toolkit for labeling DRG neuron subtypes, including CGRP^{+} subtypes
- DRG neuron subtypes exhibit distinct cutaneous axon branching patterns and areas
- DRG neuron subtypes have distinct thresholds to mechanical/thermal stimuli
- DRG neuron subtype response profiles tile mechanical and thermal stimulus space

Qi et al., 2024, Cell *187*, 1508–1526
March 14, 2024
https://doi.org/10.1016/j.cell.2024.02.006

CellPress

CellPress
OPEN ACCESS

Cell

Resource

A mouse DRG genetic toolkit reveals morphological and physiological diversity of somatosensory neuron subtypes

Lijun Qi,[1] Michael Iskols,[1] David Shi,[2] Pranav Reddy,[2] Christopher Walker,[2] Karina Lezgiyeva,[1] Tiphaine Voisin,[3] Mathias Pawlak,[4] Vijay K. Kuchroo,[4] Isaac M. Chiu,[3] David D. Ginty,[1,5,*] and Nikhil Sharma[1,2,*]

[1]Department of Neurobiology, Howard Hughes Medical Institute, Harvard Medical School, 220 Longwood Avenue, Boston, MA 02115, USA
[2]Department of Molecular Pharmacology and Therapeutics, Vagelos College of Physicians and Surgeons, Columbia University Irving Medical Center, New York, NY 10032, USA
[3]Department of Immunology, Harvard Medical School, Boston, MA 02115, USA
[4]Gene Lay Institute of Immunology and Inflammation, Brigham and Women's Hospital, Mass General Hospital, and Harvard Medical School, Boston, MA 02115, USA
[5]Lead contact
*Correspondence: david_ginty@hms.harvard.edu (D.D.G.), ns2151@cumc.columbia.edu (N.S.)
https://doi.org/10.1016/j.cell.2024.02.006

SUMMARY

Dorsal root ganglia (DRG) somatosensory neurons detect mechanical, thermal, and chemical stimuli acting on the body. Achieving a holistic view of how different DRG neuron subtypes relay neural signals from the periphery to the CNS has been challenging with existing tools. Here, we develop and curate a mouse genetic toolkit that allows for interrogating the properties and functions of distinct cutaneous targeting DRG neuron subtypes. These tools have enabled a broad morphological analysis, which revealed distinct cutaneous axon arborization areas and branching patterns of the transcriptionally distinct DRG neuron subtypes. Moreover, *in vivo* physiological analysis revealed that each subtype has a distinct threshold and range of responses to mechanical and/or thermal stimuli. These findings support a model in which morphologically and physiologically distinct cutaneous DRG sensory neuron subtypes tile mechanical and thermal stimulus space to collectively encode a wide range of natural stimuli.

INTRODUCTION

Sensory neurons of dorsal root ganglia (DRG) detect mechanical, thermal, and chemical stimuli acting on the body and transduce them into electrical impulses that are conveyed to the central nervous system (CNS). DRG neurons have a peripheral axon that extends into the skin, deep tissues, or internal organs, and another axon that projects into specific laminae of the spinal cord. DRG neuron subtypes are distinguishable by molecular, morphological, and physiological properties underlying their responses to diverse stimuli and functions. A central question in somatosensory neurobiology is how the different DRG neuron subtypes collectively encode the wide range of natural stimuli acting on the body.

Early efforts to classify DRG neurons were based on their response properties measured by nerve recordings. These foundational studies have inspired the current somatosensory neuron taxonomy. Focusing on cutaneous DRG neurons, which represent the majority of DRG neurons, those that are robustly activated by innocuous mechanical forces applied to the skin are termed low-threshold mechanoreceptors (LTMRs) and are subdivided into Aβ-, Aδ-, and C-fiber subtypes, which have fast, intermediate, and slow conduction velocities, respectively.[1] Aβ LTMR subtypes can be further subdivided by their rate of adaptation to sustained indentation of the skin. In contrast, DRG neurons with comparatively elevated mechanical force thresholds are termed high-threshold mechanoreceptors (HTMRs), and these neurons can exhibit either an A- or C-fiber conduction velocity.[2] Subsets of mechanically sensitive A- or C-fiber neurons also respond to thermal stimuli, and these neurons are often called "polymodal nociceptors"[3] or, more specifically, A- and C- mechano-heat, mechano-cold, and mechano-heat-cold neurons.[2,4,5] Alternatively, C-fiber neurons may be specifically sensitive to thermal stimuli and thus unresponsive to mechanical stimuli,[6] and these have been denoted C-fiber heat sensitive (C-Heat) or cold sensitive (C-Cold) neurons. Furthermore, a range of small molecules, including capsaicin, menthol, and histamine, can activate subsets of DRG neurons expressing the cognate receptors.[7–11] In addition to cutaneous innervation, DRG neurons can project to internal organs, with many internal organs receiving at least some component of their sensory neural innervation from DRGs.[12,13] Additionally, subtypes of skeletal muscle and tendon innervating DRG neurons contribute to proprioception.[14]

How do the physiological properties of DRG neuron subtypes overlay onto other features, such as molecular profiles, morphologies, peripheral targets, and central synaptic partners? Over the past 2 decades, the identification of marker genes, and subsequent generation of mouse reporter lines useful for selectively labeling DRG sensory neurons with defined properties, has facilitated characterization of LTMRs and other subtypes.[1,15–34] Despite these efforts, understanding the properties and functions of many DRG neuron subtypes identified using classic electrophysiological approaches has remained a challenge because of a lack of labeling strategies. Thus, genetic labeling strategies for interrogating many of the principal DRG sensory neuron subtypes are needed to advance the field.

Our ability to explore DRG sensory neuron subtypes has benefited recently by progress in genome-wide transcriptomics, in particular, large-scale sequencing of tens of thousands of single-sensory neuron transcriptomes.[28,35–39] Collectively, these sequencing studies have revealed well over a dozen transcriptionally distinct subtypes of DRG sensory neurons and the genes they express. Here, we have leveraged large-scale whole-cell transcriptomic datasets to generate a series of mouse lines and assemble a genetic toolkit for interrogating the properties and functions of DRG sensory neuron types. We report that the transcriptionally defined subtypes are distinguished by morphological and physiological properties. Moreover, functional analysis of these populations supports a population coding model of somatosensation in which DRG sensory neuron subtypes tile mechanical and thermal stimulus space to collaboratively encode the full physiological range of stimuli acting on the body.

RESULTS

A toolbox for genetic access to principal DRG neuron subtypes

We performed a large-scale single-cell RNA sequencing (scRNA-seq) analysis of DRG neurons from 3- to 4-week-old mice with the goal of using this information in conjunction with findings from a previously generated dataset[28] to identify subtype-specific genes for gaining genetic access to each principal subtype. We obtained the transcriptomes from ~40,000 DRG neurons, which were clustered and visualized by principal-component analysis (PCA)/uniform manifold approximation and projection (UMAP) analysis (Figure 1A). Consistent with previous scRNA-seq taxonomic studies of DRG neurons,[28,35,36,40,41] the dataset revealed at least 15 transcriptionally defined neuronal clusters corresponding to distinct neuronal subtypes based on previously identified sensory neuron marker genes.[15,16,19,21,25,28,40,42–53] Using this transcriptomic atlas, we sought to collate a mouse genetic toolkit that enables genetic access to each of the major transcriptionally defined DRG neuron subtypes.

We began by noting that select clusters in the scRNA-seq atlas correspond to subtypes with characterized strategies for genetic manipulation, particularly the LTMR subtypes. These include the C-LTMRs (labeled using *Th*$^{2A\text{-}CreER}$),[27] Aδ-LTMRs (*TrkB*^{CreER}),[19] Aβ RA-LTMRs (*Ret*^{CreER}),[17] and Aβ SA1-LTMRs/Aβ field-LTMRs (*TrkC*^{CreER}; E12/postnatal tamoxifen [TAM], respectively)[15] (Figure 1A; Table 1). Additionally, we noted that the cluster expressing MRGPRD is efficiently and selectively labeled using the *Mrgprd*^{CreER} allele,[30] and the cluster representing proprioceptors is labeled using the *Pvalb*^{Cre} allele.[54] Among the remaining clusters, we found that at least seven express calcitonin gene-related peptide (CGRP) alpha, a marker gene associated with nociceptors, suggesting considerable heterogeneity and presumably distinct functionalities among neurons commonly grouped as "peptidergic nociceptors." This presumed heterogeneity would be consistent with prior immunohistochemical and electrophysiological analysis of CGRP$^+$ neurons.[22–24,32,40,55,56] However, the lack of genetic tools for labeling CGRP$^+$ subtypes has impeded understanding of their properties. To taxonomize these CGRP$^+$ DRG neuron subtypes, we adopted a Greek letter nomenclature previously used (Figures 1A and S1)[28] and sought to develop mouse genetic strategies for each member of this family.

CGRP$^+$ DRG neuron subtypes have either lightly myelinated Aδ caliber axons or unmyelinated C-fibers. We first examined CGRP$^+$ neuronal clusters that were likely to have Aδ caliber axons based on the expression of neurofilament heavy chain (*Nefh*) (Figure S1B). Interestingly, we found two transcriptionally distinct putative Aδ caliber CGRP$^+$ subtypes; one (CGRP-η) is robustly labeled using a recently generated allele, *Bmpr1b*$^{T2a\text{-}Cre}$,[28] and the second putative CGRP$^+$ Aδ-fiber population (CGRP-ζ) selectively expresses the *Smr2* gene. Therefore, we generated an *Smr2*$^{T2a\text{-}Cre}$ mouse line to label this second population (Figure 1B). The other CGRP$^+$ clusters express low or undetectable levels of *Nefh* (Figure S1B) and therefore are presumably C-fiber populations. We found that two of these populations preferentially express the *Mrgpra3* and *Mrgprb4* genes, which have been the basis for the *Mrgpra3*^{Cre} and *Mrgprb4*^{Cre} driver alleles (CGRP-θ_1: Han et al.[25] CGRP-θ_2: Vrontou et al.[29]). The remaining CGRP$^+$, NEFH$^-$, and C-fiber neuron clusters did not have previously described genetic labeling strategies. Therefore, we used differential gene expression analysis to identify genes enriched in these populations and thus generated *Sstr2*$^{CreER\text{-}T2a}$ (CGRP-α), *Oprk1*$^{T2a\text{-}Cre}$ (CGRP-ε), and *Adra2a*$^{T2a\text{-}CreER}$ (CGRP-γ) alleles to label them (Figures 1A–1C).

In addition to the CGRP$^+$ neuronal clusters described above, we noted that the *Sst* gene is specifically expressed in the same cluster as *Cysltr2*[60,61]; however, we observed inefficient recombination in the DRG using a previously published *Sst*$^{IRES\text{-}Cre}$ allele (Figure S1C).[62] Likewise, previously published *Trpm8* reporter alleles either used GFP[63,64] or were BAC transgenics[65] with an uncertain degree of specificity. These considerations motivated the generation of the *Cysltr2*$^{T2A\text{-}Cre}$ and *Trpm8*$^{T2a\text{-}FlpO}$ knockin alleles to label these populations (Figures 1A and 1C).

We next tested each of the alleles (*Cysltr2*$^{T2a\text{-}Cre}$, *Trpm8*$^{T2a\text{-}FlpO}$, *Bmpr1b* $^{T2a\text{-}Cre}$, *Smr2*$^{T2a\text{-}Cre}$, *Sstr2*$^{CreER\text{-}T2a}$, *Oprk1*$^{T2a\text{-}Cre}$, and *Adra2a*$^{T2a\text{-}CreER}$) for specificity and efficiency of labeling using double smRNA-FISH to co-localize the gene used to generate the knockin allele and a recombinase-dependent reporter (Figures 1C and 1D). Consistent with specific and efficient labeling, we found robust overlap between the reporter genes labeled using the *Cysltr2*$^{T2a\text{-}Cre}$, *Trpm8*$^{T2a\text{-}FlpO}$, *Oprk1*$^{T2a\text{-}Cre}$, *Smr2*$^{T2a\text{-}Cre}$, *Sstr2*$^{CreER\text{-}T2a}$, and *Adra2a*$^{T2a\text{-}CreER}$ mouse lines and the respective cell-type-specific marker genes. However, we found that

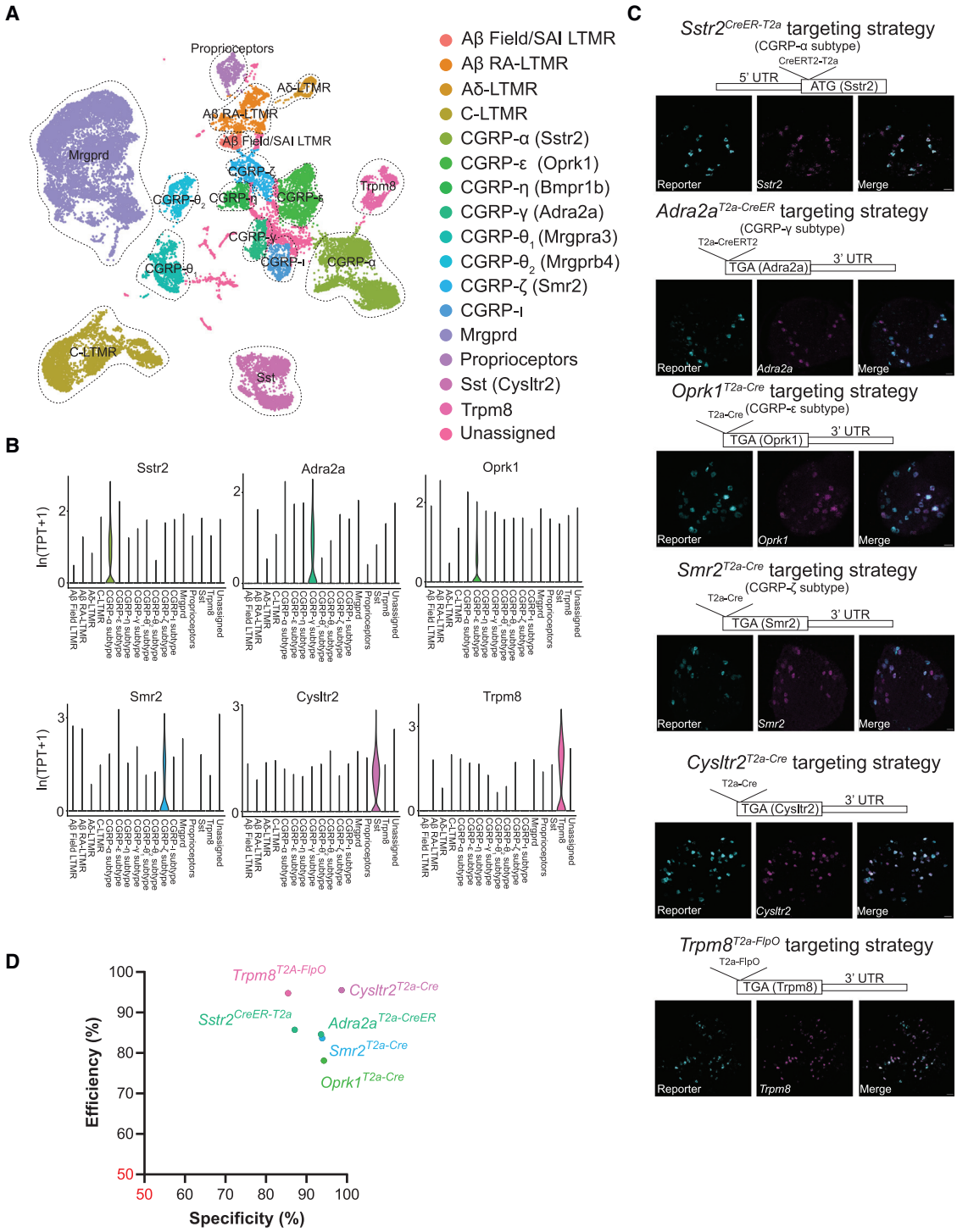

Figure 1. The transcriptional landscape of DRG sensory neurons informs the creation of tools for genetic access to neuronal subtypes

(A) UMAP visualizations of DRG scRNA-seq data alongside putative sensory neuron subtype identities.

(B) Violin plots displaying expression profiles of the marker genes used to generate mouse recombinase lines. TPT, tags per ten thousand.

(C) Targeting constructs and validation for the genetic tools using *in situ* hybridization. *Smr2*$^{T2a\text{-}Cre}$ mice were crossed to *Rosa26*$^{LSL\text{-}ReaChR}$ mice; *Trpm8*$^{T2a\text{-}FlpO}$ mice were crossed to *Avil*^{Cre}; Ai195 (*TIGRE*$^{LSL\text{-}jGCaMP7s\text{-}FSF}$) mice; the remainder were labeled using neonatal i.p. injections of an AAV carrying a Cre-dependent GFP reporter. Scale bars, 50 μm.

(D) Summary of the specificity and efficiency of the genetic tools using the labeling strategies in (C). Specificity refers to the percentage of labeled cells expressing the corresponding marker among labeled cells; efficiency refers to the percentage of labeled cells with the marker among cells expressing the marker.

See also Figures S1–S3.

Table 1. DRG somatosensory neuron genetic tools, physiological properties, and proposed nomenclature

Driver line	Cell type				
	TAM	Additional markers	Morphology	Physiology	Proposed nomenclature
Pvalb^{Cre}[54]	–	–	–	proprioceptors	proprioceptors
TrkC^{CreER}[15]	E12.5	–	Merkel-cell associated endings	Aβ SA1-LTMRs	Aβ SA1-LTMRs
	P5–P8	Ret	circumferential endings	Aβ field-LTMRs	Aβ field-LTMRs
Ret^{CreER}[17]	E10.5–E12.5	–	lanceolate endings (Pacinian corpuscles in dermis/around bones[1])	Aβ RA-LTMRs (Aβ RA2-LTMRs)	Aβ RA-LTMRs (Aβ RA2-LTMRs)
TrkB^{CreER}[19]	E12.5–P5	–	lanceolate endings (Meissner corpuscles in glabrous skin)	Aδ-LTMRs (Aβ RA1-LTMRs)	Aδ-LTMRs (Aβ RA1-LTMRs)
Th$^{2A\text{-}CreER}$[27]	P12 or later	TAFA4,[57] CD34,[34,58] Vglut3[59]	lanceolate endings	C-LTMRs	C-LTMRs
Mrgprd^{CreER}[30]	P10 or later	IB4	FNE (bushy endings)	C-HTMR/Heat	C-HTMR/HEAT (MRGPRD)
Mrgprb4^{Cre}[29]	–	–	FNE (bushy endings)	C-HTMR/Heat	C-HTMR/Heat (MRGPRB4)
Mrgpra3^{Cre}[25]	–	–	FNE	C-HTMR/Heat	C-HTMR/Heat (MRGPRA3)
Bmpr1b$^{T2A\text{-}Cre}$[28]	–	CGRP	circumferential endings	Aδ-HTMR	Aδ-HTMR (BMPR1B)
Sstr2$^{T2a\text{-}CreER}$	P12 or later	CGRP	FNE	C-Heat	C-Heat (SSTR2)
Smr2$^{T2a\text{-}Cre}$	–	CGRP	FNE (large arborization)	Aδ-HTMR/Heat	Aδ-HTMR/Heat (SMR2)
Cysltr2^{Cre}	–	SST,[60] NPPB,[31] IL31RA[60,61]	FNE	C-HTMR/Heat	C-HTMR/Heat (CYSLTR2/SST)
Trpm8$^{T2a\text{-}Flpo}$	–	–	FNE	C-Cold	C-Cold (TRPM8)
Adra2a$^{T2a\text{-}CreER}$	P14–P16	CGRP	non-cutaneous	unknown	–

TAM, tamoxifen; FNE, free-nerve ending.

reporter gene expression in *Oprk1*$^{T2a\text{-}Cre}$ animals was not restricted to C-fiber CGRP^{+} DRG neurons (Figures 1A, S1D, and S1E). Furthermore, morphological analysis of cutaneous axonal endings of neurons labeled using *Oprk1*$^{T2a\text{-}Cre}$ mice showed significant heterogeneity (Figure S1G), consistent with a previous study.[24,66] Therefore, the *Cysltr2*$^{T2a\text{-}Cre}$, *Trpm8*$^{T2a\text{-}FlpO}$, *Bmpr1b* $^{T2a\text{-}Cre}$, *Smr2*$^{T2a\text{-}Cre}$, *Sstr2*$^{CreER\text{-}T2a-}$, and *Adra2a*$^{T2a\text{-}CreER}$ mouse lines, but not *Oprk1*$^{T2a\text{-}Cre}$, were used in subsequent analyses.

With mouse genetic strategies now available for labeling most transcriptionally distinct clusters, we next sought to assess their neurochemical and histological properties. Interestingly, DRG neurons labeled using the *Adra2a*$^{T2a\text{-}CreER}$ (CGRP-γ) allele stood out in initial analyses because they exhibited a striking difference in their prevalence across different axial levels (Figure S2A), with restricted labeling in lower thoracic and L6-S1 level. Moreover, little to no axonal labeling was observed in the skin of the limbs and trunk in these mice (Figure S2B); however, robust labeling of terminals in internal organs, including the bladder (Figure S2C) and colon,[67] was observed. Thus, CGRP-γ neurons selectively innervate internal organs but not skin.

To begin classifying neurons labeled by each genetic strategy, we co-localized established neurochemical markers commonly used to label DRG subtypes with reporter gene expression to visualize the cell bodies of the labeled neurons from each of the mouse lines described above. This was achieved by expressing a recombinase-dependent fluorescence reporter in DRG neurons via a *Rosa26* reporter allele or neonatal intraperitoneal injection of adeno-associated viruses (AAV). The reporter signals detected in DRG neuron cell bodies were compared with signals for three neurochemical makers: CGRP, which labels many small and large diameter "peptidergic" DRG neurons; Isolectin B4 (IB4), which labels a subset of small-diameter "non-peptidergic" C-fiber neuron subtypes; and NEFH, which labels medium and large diameter neurons representing myelinated subtypes. This analysis revealed that the genetic approaches used to label clusters assigned as Aβ- and Aδ-LTMRs have large or medium diameter, NEFH^{+} and CGRP^{-}/IB4^{-} cell bodies, as expected. Also consistent with prior measurements, C-LTMRs are small-diameter, CGRP^{-}/IB4^{-} neurons (Figures S3A, S3C, and S3D).[16,59] The genetically labeled MRGPRD^{+} neurons, CYSLTR2^{+} neurons, and TRPM8^{+} neurons exhibited small-diameter cell bodies that are CGRP^{-}/NEFH^{-} (Figures S3A–S3D), also as expected.[30,60,63] Notably, whereas MRGPRD^{+} neurons were IB4^{+}, CYSLTR2^{+} neurons, and TRPM8^{+} neurons exhibited little overlap with IB4 (Figures S3A and S3C). Interestingly, although MRGPRA3^{+} and MRGPRB4^{+} populations were NEFH^{-}, as expected[25,68,69] (Figures S3B and S3C), both populations showed less overlap than expected with CGRP, which contrasts with the expression of CGRP transcripts observed by scRNA-seq (Figure S1B); the mismatch in CGRP mRNA and protein in these subtypes may be due to differences in translation. We note that *Mrgprb4*^{Cre} labels several distinct DRG populations.[68] We postulate that multiple subtypes express Cre recombinase at different developmental times, leading to genetic labeling of the sum of all populations that express *Mrgprb4*^{Cre} at any point in the life of the animal when crossed to a reporter line. To mitigate such summated labeling, we introduced Cre-dependent reporters via postnatal AAV injections into *Mrgprb4*^{Cre} animals and harvested tissue within 3–4 weeks, when possible. The

CGRP-α cluster neurons labeled using *Sstr2*$^{CreER\text{-}T2a}$ were CGRP^{+}, but IB4^{-} and NEFH^{-}, and exhibited small-diameter cell bodies (Figures S3A–S3D). It is notable that despite the CGRP-α population being the most numerous CGRP^{+} subtype, specific markers for this population have not been previously described. Lastly, the CGRP-η (BMPR1B^{+}) and CGRP-ζ (SMR2^{+}) populations were CGRP^{+}, IB4^{-}, and moderately NEFH^{+}, consistent with the likelihood that both populations are lightly myelinated with an Aδ conduction velocity (Figures S3A–S3D).

Taken together, our transcriptomic efforts combined with a series of mouse alleles generated in this study (*Cysltr2*^{Cre}, *Trpm8*$^{T2a\text{-}FlpO}$, *Smr2*$^{T2a\text{-}Cre}$, *Sstr2*$^{CreER\text{-}T2a}$, *Adra2a*$^{T2a\text{-}CreER}$, and *Bmpr1b*$^{T2a\text{-}Cre}$) and previously reported alleles (*Th*$^{T2A\text{-}CreER}$, *TrkB*^{CreER}, *TrkC*^{CreER}, *Ret*^{CreER}, *Pvalb*^{Cre}, *Mrgprd*^{CreER}, *Mrgpra3*^{Cre}, and *Mrgprb4*^{Cre}) have led to the curation of a genetic resource useful for labeling and manipulating most of the transcriptionally distinct DRG neuron populations found in mice (Table 1).

Skin innervation patterns and morphological reconstructions of DRG sensory neuron subtypes

We next used the genetic labeling strategies to test the hypothesis that each transcriptionally distinct DRG neuron subtype exhibits a distinguishable morphology. We visualized the cutaneous endings of the labeled DRG neuron subtypes with single-neuron resolution by performing sparse labeling using the array of driver lines with whole-mount alkaline phosphatase (AP) staining of hairy skin. This approach revealed Aβ SAI-LTMRs innervated only one or two clusters of Merkel cells (touch domes), whereas individual Aβ RA-LTMRs, Aδ-LTMRs, and C-LTMRs branched much more extensively and formed lanceolate endings surrounding dozens of hair follicles (Figures 2A, 2E, and 2F), consistent with previous reports.[15,70] Also, consistent with prior findings, individual Aβ field-LTMRs exhibited expansive morphological receptive fields and formed circumferential endings associated with many hair follicles (Figures 2B, 2E, and 2F).[15] Single-neuron reconstructions of MRGPRD^{+} neurons revealed a "bushy ending" morphology, with densely packed clusters often embedding circumferential-like endings near hair follicles (Figures 2C and S4A), in line with a previous report.[30] Most MRGPRB4^{+} neurons, labeled by injection of AAV expressing Cre-dependent AP at 3–4 weeks old, also have bushy endings but with larger arborizations compared with MRGPRD^{+} neurons,[20,71] whereas MRGPRA3^{+} neurons exhibited an even larger terminal area with less dense branching (Figures 2C, 2E, 2G, and S4). Thus, the MRGPRD^{+}, MRGPRB4^{+}, and MRGPRA3^{+} neurons exhibited related but quantitatively distinguishable morphologies (Figures S4D and S4E). In comparison, the "free nerve endings" (FNEs) formed by individual CYSLTR2^{+} neurons and TRPM8^{+} neurons exhibited distinct branching patterns, with many fewer branches than the bushy endings (Figures 2C and 2G).

Individual SSTR2^{+} neurons exhibited relatively few branches and widely spaced axon terminals across their arborization area (Figures 2C, 2G, and S4A). Individual BMPR1B^{+} neurons, in contrast, formed circumferential endings associated with hair follicles at a quantity double that of Aβ field-LTMRs, and this corresponded to larger anatomical receptive fields than Aβ field-LTMRs (Figures 2B, 2E, and 2F). Thus, the circumferential endings of BMPR1B^{+} neurons and Aβ field-LTMRs have large innervation areas, with BMPR1B^{+} neurons being the largest among the hair follicle-associated afferents (Figures 2E and 2F). Finally, SMR2^{+} neurons exhibited expansive morphological receptive fields with sparse branches (Figures 2D, 2E, 2G, and S4A–S4C). Neurons in the SMR2^{+} population formed the largest anatomical receptive fields among the entire cohort of DRG neuron subtypes, reaching areas up to 30 mm^2 (Figure 2E).

We also expressed a fluorescent reporter in each cutaneous subtype and performed immunostaining in hairy skin samples to assess the extent to which they terminate in association with hair follicles, in the dermis, or the epidermis. As expected, Aβ RA-LTMRs, Aδ-LTMRs, and C-LTMRs all form lanceolate endings associated with hair follicles (Figure S5B),[1,16,19] whereas BMPR1B^{+} neuron terminals formed circumferential endings. On the other hand, MRGPRD^{+}, CYSLTR2^{+}, MRGPRB4^{+}, MRPGRA3^{+}, TRPM8^{+}, SSTR2^{+}, and SMR2^{+} neurons terminated as FNEs within the epidermis (Figure S5). The finding that SMR2^{+} neurons are a major population of A-fiber CGRP^{+} fibers that penetrate the epidermis stands in contrast to the commonly held assumption that CGRP^{+} neurons that innervate the epidermis are C-fibers.

Thus, across the transcriptionally distinct subtypes, there exists a remarkably large range of terminal morphologies and branching patterns, with each genetically defined cutaneous DRG neuron subtype exhibiting a different morphology.

A comparison of the central projection patterns across DRG sensory neuron subtypes

In addition to the morphological diversity of their cutaneous endings, many DRG neuron subtypes are distinguished by their central projections. We performed immunostaining of spinal cords from genetically labeled mice using antibodies against the reporter, CGRP, and IB4. Beginning superficially, TRPM8^{+} neurons terminated within the most dorsal region of the dorsal horn, immediately superficial to CGRP^{+} fibers of lamina I (Figures 3A–3C).[72] Terminals of SSTR2^{+} neurons, BMPR1B^{+} neurons, and SMR2^{+} neurons were primarily located in lamina I and IIo, with some BMPR1B^{+} and SMR2^{+} terminals also observed in deeper lamina (Figures 3B and 3C). Continuing deeper in the dorsal horn, the CYSLTR2^{+}, MRGPRA3^{+}, MRGPRB4^{+}, and MRGPRD^{+} populations terminated primarily in lamina IIi, overlapping with the layer of IB4 (Figures 3B and 3C).[21] Then, deeper in the dorsal horn, C-LTMR terminals were concentrated in lamina IIiv, Aδ-LTMR axons were observed in lamina IIiv and lamina III, and Aβ RA-LTMRs terminated in lamina III–IV (Figures 3B and 3C), consistent with prior reports.[16,27,59,73] Therefore, the central terminals of transcriptionally distinct DRG neuron subtypes elaborate within defined domains of the spinal cord (Figures 3B and 3C).

Taken together, the DRG subtypes genetically labeled using the curated genetic toolkit exhibited distinct cell body sizes, neurochemical properties, cutaneous morphologies, branching patterns, and central termination zones. These findings underscore the selectivity and utility of the cutaneous DRG neuron mouse genetic toolkit (Table 1).

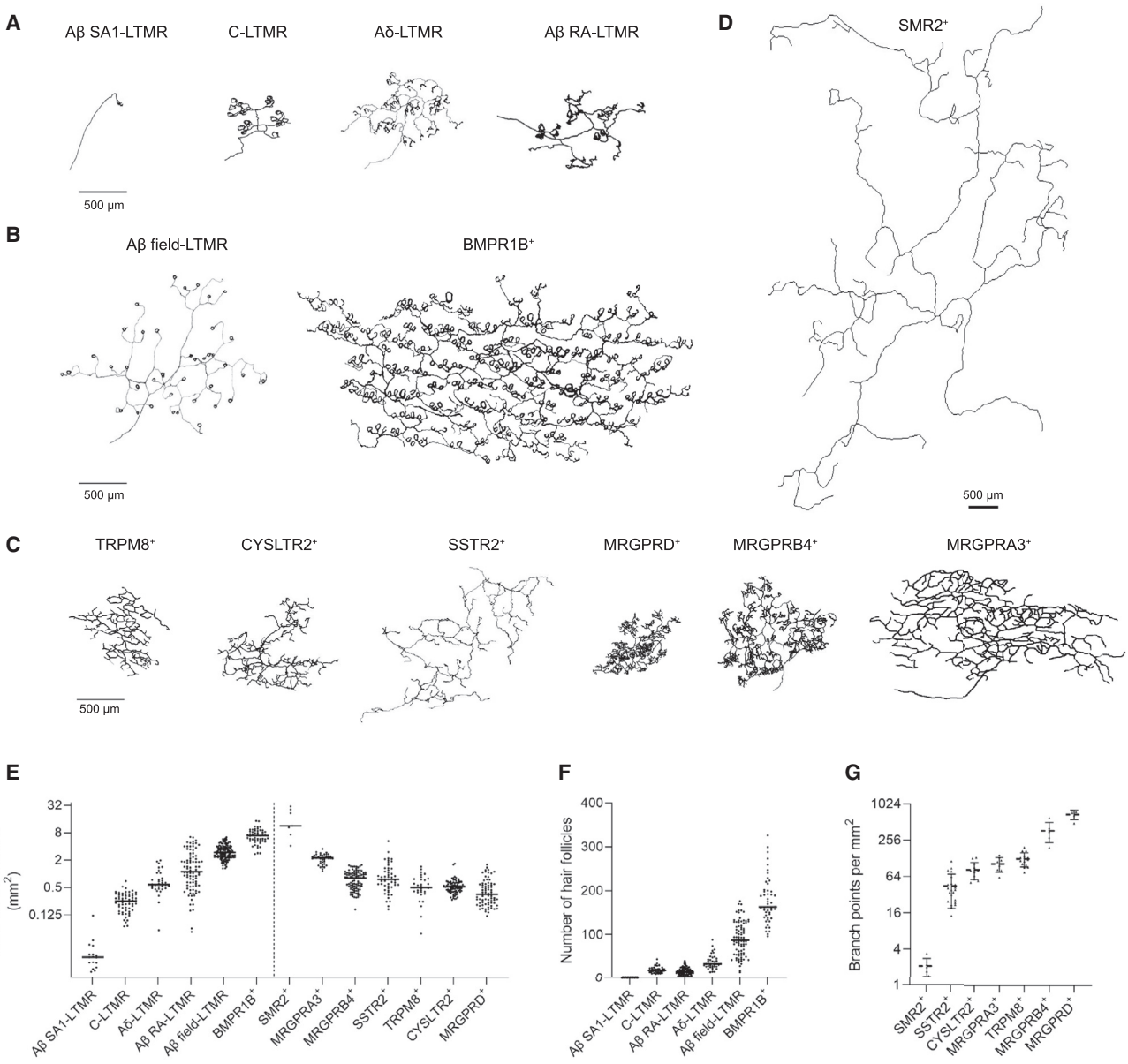

Figure 2. Morphological diversity of genetically labeled DRG subtypes revealed by sparse labeling

(A) Reconstructed examples of hairy skin whole-mount AP staining of a single Aβ SAI-LTMR labeled using *TrkC*^{CreER}, an Aβ RA-LTMR labeled using *Ret*^{CreER}, an Aδ-LTMR labeled using *TrkB*^{CreER}, and a C-LTMR labeled using *TH*$^{2A\text{-}CreER}$. All the driver lines in (A) are crossed to *Brn3a*^{cKOAP}.

(B) Reconstructed examples of an Aβ field-LTMR labeled using *TrkC*^{CreER}, *Brn3a*^{cKOAP}, and a CGRP-η neuron labeled using *Bmpr1b*^{Cre} (AAV-CAG-FLEX-PLAP injection into hairy skin).

(C) Reconstructed examples of free-nerve endings of individual TRPM8$^+$, CYSLTR2$^+$, SSTR2$^+$, MRGPRD$^+$, MRGPRB4$^+$, and MRGPRA3$^+$ neurons. See STAR Methods for sparse labeling approaches.

(D) Reconstructed examples of free nerve endings of an SMR2$^+$ neuron.

(E) Summary of anatomical receptive field sizes of genetically labeled DRG neuron subtypes. The dashed line separates the hair follicle-associated endings and the free-nerve endings. The scale of the y axis is $\log_2$. n = 17, 35, 63, 90, 125, 54, 7, 40, 95, 53, 18, 84, and 76 (from left to right). Images of each subtype were obtained from more than 3 animals, 4–5 weeks old.

(F) Summary of number of hair follicles innervated by individual neurons of different subtypes. n = 7, 37, 45, 89, 86, and 50, left to right.

(G) Summary of branching density of free nerve ending neurons. n = 7, 22, 12, 15, 6, and 5, from left to right. All scale bars, 500 μm (A–D). The data for Aβ SAI-LTMRs, Aβ RA-LTMRs, and Aβ field-LTMRs are replotted or reconstructed from Bai et al.[15]

See also Figures S4 and S5.

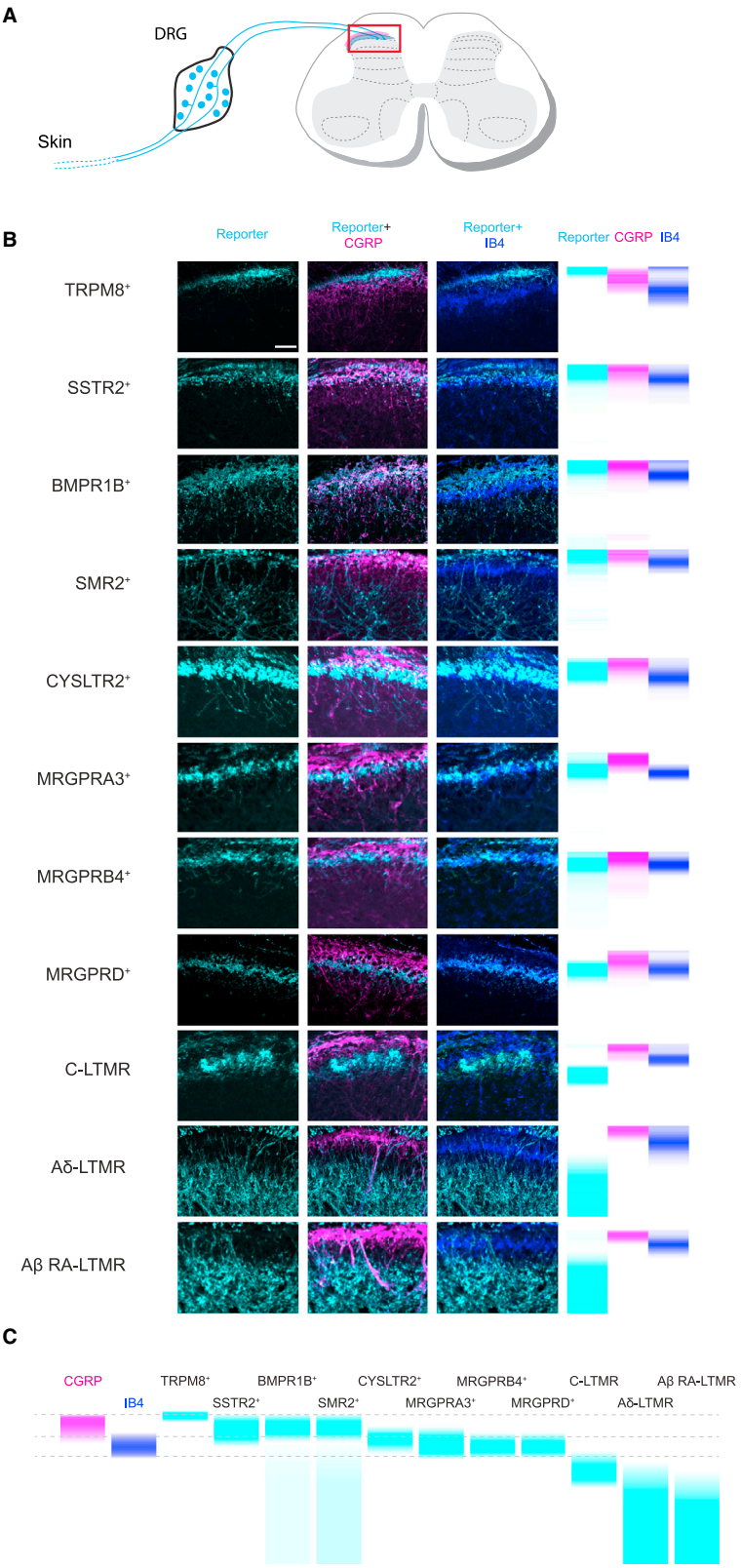

Figure 3. Characterization of the spinal cord terminals of genetically labeled cutaneous DRG subtypes

(A) Schematics of central projections of DRG neurons. The red frame refers to the region of interest shown in (B).

(B) Representative images of central terminals in lumbar spinal cord of genetically labeled cutaneous DRG subtypes, co-stained with CGRP and IB4. The right column shows quantification of the depth of spinal cord terminals relative to CGRP and IB4 signal. *Trpm8*$^{T2a\text{-}FlpO}$ were crossed to *Avil*^{CreER}; Ai65 mice; *TrkB*^{CreER} and *Ret*^{CreER} were crossed to *Advillin*^{FlpO}; Ai65 mice; the remainder were labeled using neonatal i.p. injections of an AAV carrying a Cre-dependent GFP reporter. All images are of the same scale. Scale bars, 50 μm. Depth quantifications are from spinal sections from over three animals per subtype.

(C) Comparison of axon terminal depth for the cutaneous DRG subtypes, relative to CGRP- and IB4-labeled axons.

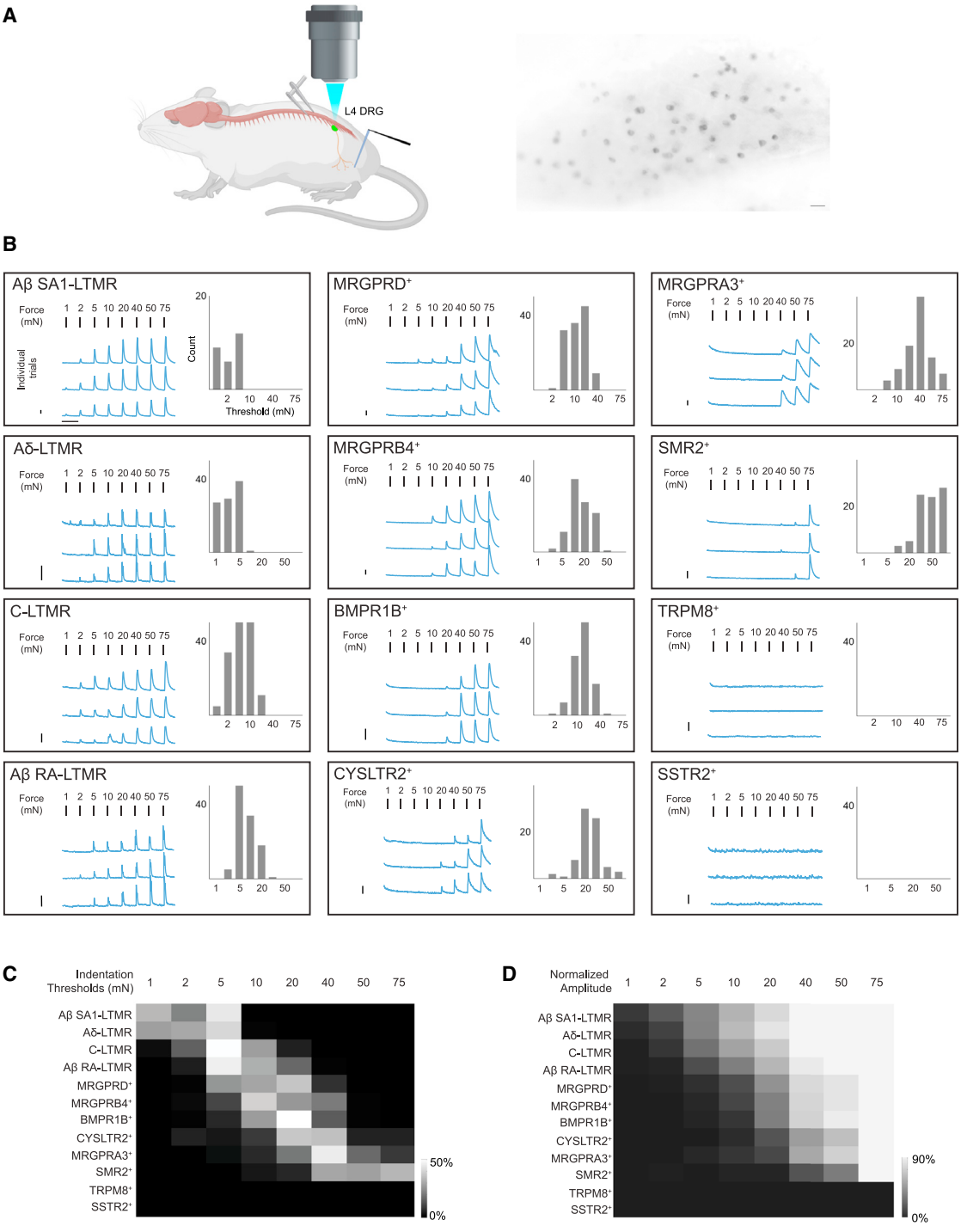

Figure 4. Indentation force space is tiled by the different mechanical thresholds of DRG neuron subtypes

(A) Left: schematic of *in vivo* DRG calcium imaging and the indentation stimulus. Right: representative field of view from $Th^{2A\text{-}CreER}$; Ai148 (baseline fluorescence, scale bar, 50 μm). To express GCaMP in distinct DRG subtypes, $Bmpr1b^{T2a\text{-}Cre}$ mice were crossed to Ai95; $MrgprA3^{Cre}$ mice were crossed to Ai96; $Trpm8^{T2a\text{-}FlpO}$ mice were crossed to $Avil^{Cre}$; Ai195; other recombinase mouse lines were crossed to Ai148.

(B) Representative calcium signals and threshold distributions for each DRG neuron subtype responding to 0.5-s step indentations. Left in each box: traces from a total of three trials for the same example neuron (scale bars: 20% ΔF/F, y axis; 10 s, x axis). Right in each box: number of traces with indicated threshold.

(legend continued on next page)

Indentation force space is tiled by the force thresholds of at least 10 DRG neuron subtypes

We next compared the mechanical and thermal response properties across the transcriptionally and morphologically distinct cutaneous DRG neuron types. For this analysis, *in vivo* calcium imaging of L4 DRG neurons was performed using the relevant recombinase driver lines in conjunction with GCaMP reporters (Figure 4A). We started by examining the mechanical sensitivity of DRG subtypes innervating thigh hairy skin, using step indentations of the skin with a 200-μm-diameter indenter tip to deliver forces ranging from 1 to 75 mN to the receptive fields of neurons (Figure 4A). These measurements allowed for a quantitative and direct comparison of indentation response thresholds and adaptation properties across the cutaneous DRG neuron subtypes.

We found that Aβ RA-LTMRs, Aβ SAI-LTMRs, Aδ-LTMRs, and C-LTMRs innervating hairy skin all exhibited low-threshold (<10 mN, 200-μm indenter tip) activation, as expected. Specifically, Aβ SAI-LTMRs, Aδ-LTMRs, and C-LTMRs showed exquisite mechanical sensitivity, with most neurons responding at ~1–5-mN indentation force (Figures 4B and 4C). Aβ RA-LTMRs had slightly higher thresholds in general, but most responded in the low-threshold range (≤10 mN) (Figures 4B and 4C). Each of these four LTMR subtypes exhibited graded increases in responses in the low-force range and plateaued between 20 and 40 mN (Figures 4D and S6C).

In contrast, MRGPRD$^+$ and MRGPRB4$^+$ neurons showed graded responses over a broader range of mechanical forces, with most neurons exhibiting force thresholds between 5 and 20 mN, which is in the low-to-medium force-intensity range (Figures 4B–4D). The BMPR1B$^+$ neurons exhibited slightly higher force thresholds, mostly around 20 mN. The thresholds of CYSLTR2$^+$ neurons and MRGPRA3$^+$ neurons were higher still, in the 20–40 mN range. SMR2$^+$ neurons exhibited the highest force thresholds, responding primarily to forces greater than 40 mN (Figures 4B and 4C). Lastly, TRPM8$^+$ neurons and SSTR2$^+$ neurons were unresponsive to mechanical indentations at all forces tested (Figures 4B–4D); their viability and responsivity was confirmed by electrical stimulation of the skin. Thus, considering their thresholds in the medium-to-high force range and their preferential responses to elevated (>40 mN) mechanical forces (Figures 4C, 4D, and S6C), at least six DRG neuron populations, the MRGPRD$^+$, MRGPRB4$^+$, BMPR1B$^+$, CYSLTR2$^+$, MRGPRA3$^+$, and SMR2$^+$ neurons, fall into the "HTMR" category, or the "nociceptor" category based on the classical nociceptor definition.[2,3]

We also asked whether the subtypes exhibit transient or sustained responses to static indentation of the skin. For this, a complementary series of mechanical indentation experiments was done in which the duration of skin indentation time was extended to 3 s (Figure S6A). We observed that nearly all Aδ-LTMRs responded during both the onset and offset of indentations but not during the sustained indentation period, as expected,[1] and most Aβ RA-LTMRs (29/36) also responded during the onset and offset of step indentations with a subset (7/36) responding only at stimulus onset (Figure S6B). In contrast, Aβ SAI-LTMRs exhibited sustained calcium signals with large amplitudes for the duration of the indentation step, also as expected.[1] We further observed that C-LTMRs had an intermediate rate of adaptation, with large responses observed at both the onset and offset of the stimulus and a slow decrease of the calcium signal during the sustained phase (Figure S6B), also in line with previous measurements.[16,59] By contrast, each of the six HTMR subtypes (MRGPRD$^+$, MRGPRB4$^+$, BMPR1B$^+$, CYSLTR2$^+$, MRGPRA3$^+$, and SMR2$^+$ neurons) exhibited sustained calcium responses during the entire step indentation period (Figure S6B), suggesting that each of the six HTMR subtypes is slowly adapting to sustained indentation of the skin.

Responsivity of the subtypes to several additional mechanical stimuli was also assessed (Figure 5). For this, the skin was stimulated using an air puff (1 PSI), gentle stroke using a cotton tip, pinch with round-tip forceps, and indentation with Von Frey filaments. Thermal stimuli were also applied using a custom-made Peltier device contacting the same area of skin that received the mechanical stimuli. Three of the LTMR subtypes (Aβ RA-LTMRs, Aδ-LTMRs, and C-LTMRs) were tested in this analysis, and they exhibited responses to both air puff and cotton swab stroke elicited robust responses (Figures 5A–5C), as expected. Consistent with the idea that LTMRs saturate in the innocuous range (Figures 4D and S6C),[1] these LTMR populations reached maximum activation by the stroke stimulus (Figure 5C), with pinch showing no greater level of activation. As with the LTMRs, three HTMR populations, BMPR1B$^+$ neurons, MRGPRB4$^+$ neurons, and MRGPRD$^+$ neurons, were also activated by skin stroke. However, in contrast to the LTMRs, these three populations exhibited a higher degree of activation by pinch (Figures 5C and 5D), reflecting their wide dynamic range of mechanosensitivity (Figures 4C and 4D). The CYSLTR2$^+$ neurons, MRGPRA3$^+$ neurons, and SMR2$^+$ neurons showed much higher activation by pinch than stroke, but their responses to pinch were smaller than their responses to thermal stimuli, on average (Figures 5A, 5C, 5D, and 7). Lastly, TRPM8$^+$ and SSTR2$^+$ exhibited weak or no responses to any mechanical stimulus, including pinch and Von Frey filaments of up to 26 g (Figures 5A and 5C), consistent with the step indentation analysis (Figures 4B–4D and S6B), indicating that these populations are mechano insensitive.

In summary, 10 of the transcriptionally distinct cutaneous DRG neuron subtypes tested here encode stimulus intensity across a range of innocuous to noxious mechanical forces, with individual subtypes specialized at encoding within a distinct force range. Two other DRG neuron subtypes are mostly mechano-insensitive. Interestingly, when considered as a collective, the transcriptionally distinct DRG mechanoreceptor

(C) Summary of threshold distributions for each DRG neuron subtype across the range of indentation forces. The percentage of trials with a corresponding threshold are coded by brightness levels. Percentages for TRPM8$^+$ and SSTR2$^+$ neurons, which did not respond to indentation, were set to zero.
(D) Summary of average response amplitudes for each DRG subtype across the range of indentation forces. The response amplitudes (ΔF/F) were normalized to responses at 75 mN for each neuron and then averaged for each subtype. The normalized amplitudes for TRPM8$^+$ and SSTR2$^+$ neurons were set to zero, as in (C).
See also Figure S6.

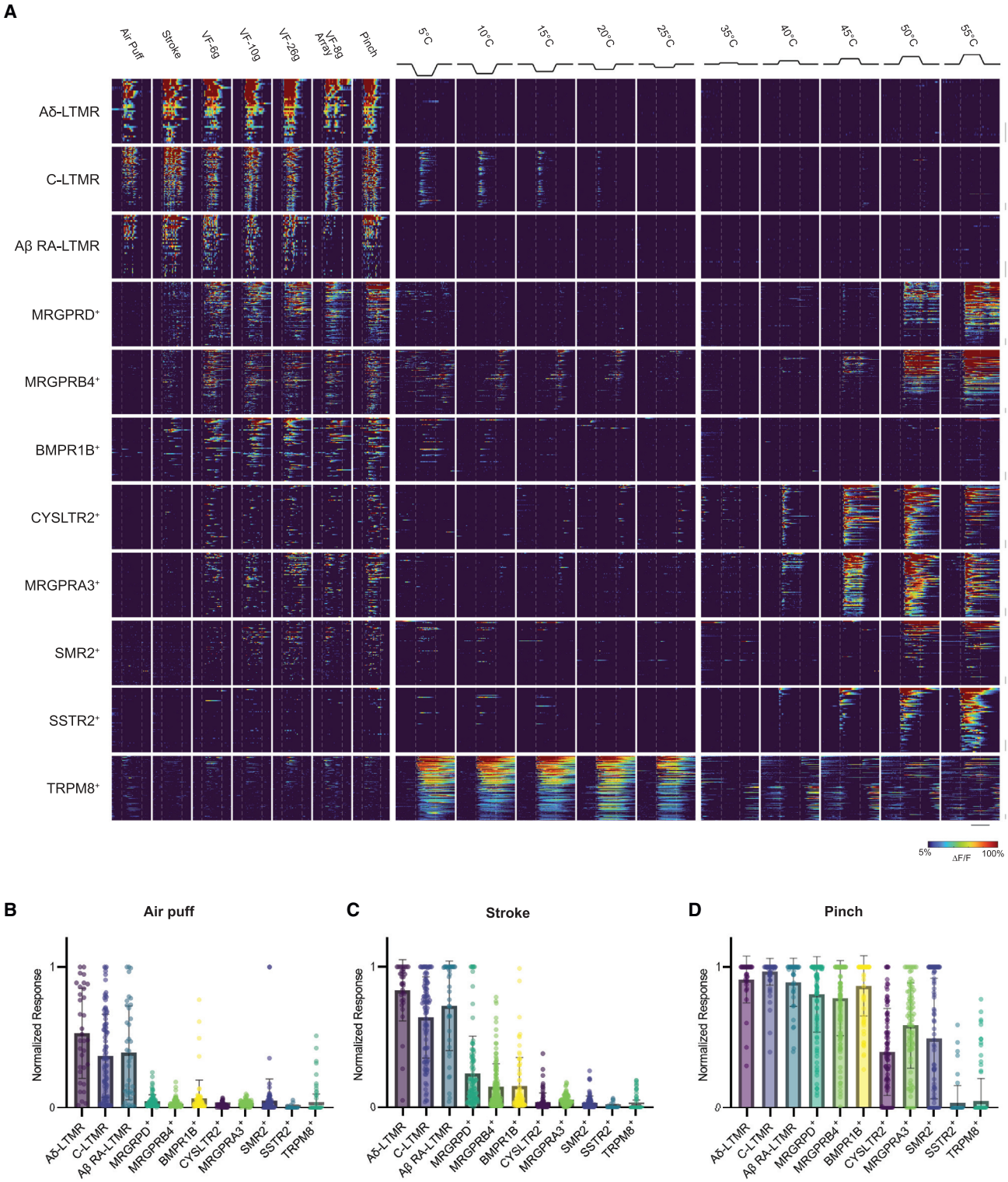

Figure 5. Responses to diverse mechanical and thermal stimuli by distinct DRG neuron subtypes

(A) Heatmaps of calcium signals under a range of mechanical and thermal stimuli. VF-6 g, VF-10 g, and VF-26 g refer to 6-, 10-, and 26-g Von Frey filaments. VF-8g-Array refers to an array (5 × 5) of custom made 8-g Von Frey hair covering the same area as the Peltier device (see STAR Methods). Baseline temperature:

(legend continued on next page)

subtypes tile the physiological range of indentation force thresholds (Figure 4C). These observations are consistent with a population coding scheme, in which an increasing number of LTMR and HTMR subtypes are recruited as skin indentation intensity increases.

Temperature is represented as absolute or relative by different sensory neuron subtypes

Thermal responsivity of the cutaneous DRG neuron subtypes was assessed by probing the same skin regions with precise thermal stimuli delivered using a custom-built Peltier system. A series of temperature steps were delivered, starting from physiological skin surface temperature (32°C), and then ramping (5°C s^{-1}) and holding (20 s) at a target temperature between 5°C and 55°C. The temperature was then reverted to physiological skin surface temperature, again at a rate of 5°C s^{-1} (Figure S6D). The temperature steps were delivered sequentially, beginning with innocuous and then into the noxious range, with alternating presentations of heat and cold stimuli.

We observed that the cooling of the skin activated both TRPM8$^+$ neurons and C-LTMRs; however, the responses of these two populations were highly distinct. TRPM8$^+$ neurons exhibited heightened activity throughout the duration of the cooling epoch, as well as high sensitivity to even moderately cool temperatures (Figures 5A, 6A, and 6C); in contrast, C-LTMRs responded exclusively during temperature decreases (Figures 5A and 6C). These observations are consistent with prior observations that C-LTMRs are activated during cooling of the skin.[16,59,74] We also observed that the TRPM8$^+$ and C-LTMR populations responded to temperature decreases from warm/heat to baseline (32°C), although with smaller amplitudes compared with cooling below 32°C (Figure 6C). Intriguingly, ~40% of TRPM8$^+$ neurons exhibited a reduction in GCaMP signal by warmth (Figure 6C), suggesting that this population is tonically active at physiological skin temperatures, consistent with recent reports.[6,75] Thus, both the TRPM8$^+$ and C-LTMR populations can encode relative change of temperatures. We also note that no single discrete DRG neuron subtype exclusively encodes noxious cold (<15°C). Rather, responses to noxious cold temperatures were distributed across multiple subtypes, including subsets of SMR2$^+$, TRPM8$^+$, BMPR1B$^+$, MRGPRD$^+$, MRGPRB4$^+$, and SSTR2$^+$ neurons (Figure 5A).

Conversely, seven of the transcriptionally defined DRG neuron populations responded to elevations in skin temperature: SSTR2$^+$, MRGPRD$^+$, MRGPRB4$^+$, MRGPRA3$^+$, CYSLTR2$^+$, SMR2$^+$ neurons, and a subset of TRPM8$^+$ neurons (Figures 6A–6E). The MRGPRD$^+$, MRGPRB4$^+$, and SMR2$^+$ neurons were reliably activated by noxious heat (≥45°C), whereas many SSTR2$^+$ neurons and MRGPRA3$^+$ neurons had thresholds of ~40°C (Figures 5A and 6A); neurons in these populations exhibited sustained activation throughout the duration of the stimulation period (Figure 5A). CYSLTR2$^+$ neurons were most sensitive to innocuous warm temperatures (35°C–40°C) (Figure 6A), although subsets of MRGPRA3$^+$, MRGPRB4$^+$, MRGPRD$^+$, and SSTR2$^+$ populations also responded to warm temperatures. Interestingly, subsets of CYSLTR2$^+$ (33%), MRGPRB4$^+$ (38%), and MRGPRA3$^+$ (35%) neurons were activated transiently during increases in temperature (Figure 6D), especially from cold to baseline, suggesting that these neurons are activated by relative temperature elevation in addition to absolute temperature.

These findings are consistent with a multipronged strategy for the encoding of thermal stimuli; individual DRG neuron subtypes encode either a decrease or increase in skin temperature. Within these categories, subtypes are either responsive to transitions in temperature or the absolute temperatures of the skin surface.

Polymodality of transcriptionally distinct DRG neuron subtypes

By comparing responses to mechanical and thermal stimuli in the same neuronal populations, we were able to quantitatively assess the extent of polymodality within each genetically labeled population.[76] This analysis revealed that virtually all Aβ RA-LTMRs, Aδ-LTMRs, and the majority of BMPR1B$^+$ neurons were tuned to mechanical but not thermal stimuli. C-LTMRs were sensitive to cooling but most prominently activated by mechanical stimuli (Figure 7A). Nearly all MRGPRD$^+$, MRGPRB4$^+$, MRGPRA3$^+$, CYSLTR2$^+$, and SMR2$^+$ neurons were polymodal, sensitive to both mechanical and thermal stimuli (Figure 7B).[25,77–79] In contrast, SSTR2$^+$ and TRPM8$^+$ neurons were sensitive to thermal but not mechanical stimuli (Figure 7C).

Importantly, these functional analyses enable alignment of the classical physiology-based descriptions of neuronal populations[2] with the transcriptionally distinct neuronal subtypes. Therefore, the classical physiology-based nomenclature used for the LTMRs (C-LTMRs, Aδ-LTMRs, Aβ RAI-LTMRs, Aβ RAII-LTMRs, Aβ SA-LTMRs, and Aβ field-LTMRs) can now be extended to the other subtypes of cutaneous DRG neurons. This classification uses "C" or "A" for fiber conduction velocity, followed by the terms LTMR, HTMR, and/or Cold and Heat. Thus, C-fiber types classified using this proposed nomenclature are C-HTMR/Heat (MRGPRD), C-HTMR/Heat (MRGPRB4), C-HTMR/Heat (MRGPRA3), C-HTMR/Heat (CYSLTR2/SST), C-Cold (TRPM8), and C-Heat (SSTR2). The A-fiber HTMR subtypes are Aδ-HTMR (BMPR1B) and Aδ-HTMR/Heat (SMR2) (Table 1).

DISCUSSION

Defining the properties and functions of primary DRG sensory neurons is fundamental for understanding somatosensation. Accomplishing this requires phenotypic analysis of the principal DRG sensory neuron subtypes, across multiple levels of analysis.[80] Here, we used transcriptomic measurements of the mouse DRG to guide the assembly of an array of mouse lines

32°C. Each row of the heatmap represents responses of an individual neuron. The vertical scale bars on the right refer to 10 neurons. The horizontal scale bar represents 20 s.

(B–D) Summaries of response amplitudes (ΔF/F) for air puff (B), stroke (C), and pinch (D) stimuli, normalized to each neuron's maximum responses to all stimuli. Neuron counts from left to right are 33, 91, 38, 98, 131, 71, 81, 81, 89, 58, and 128. Neurons of each subtype were imaged from 3 to 5 animals, age 4–6 weeks. Error bars, SD.

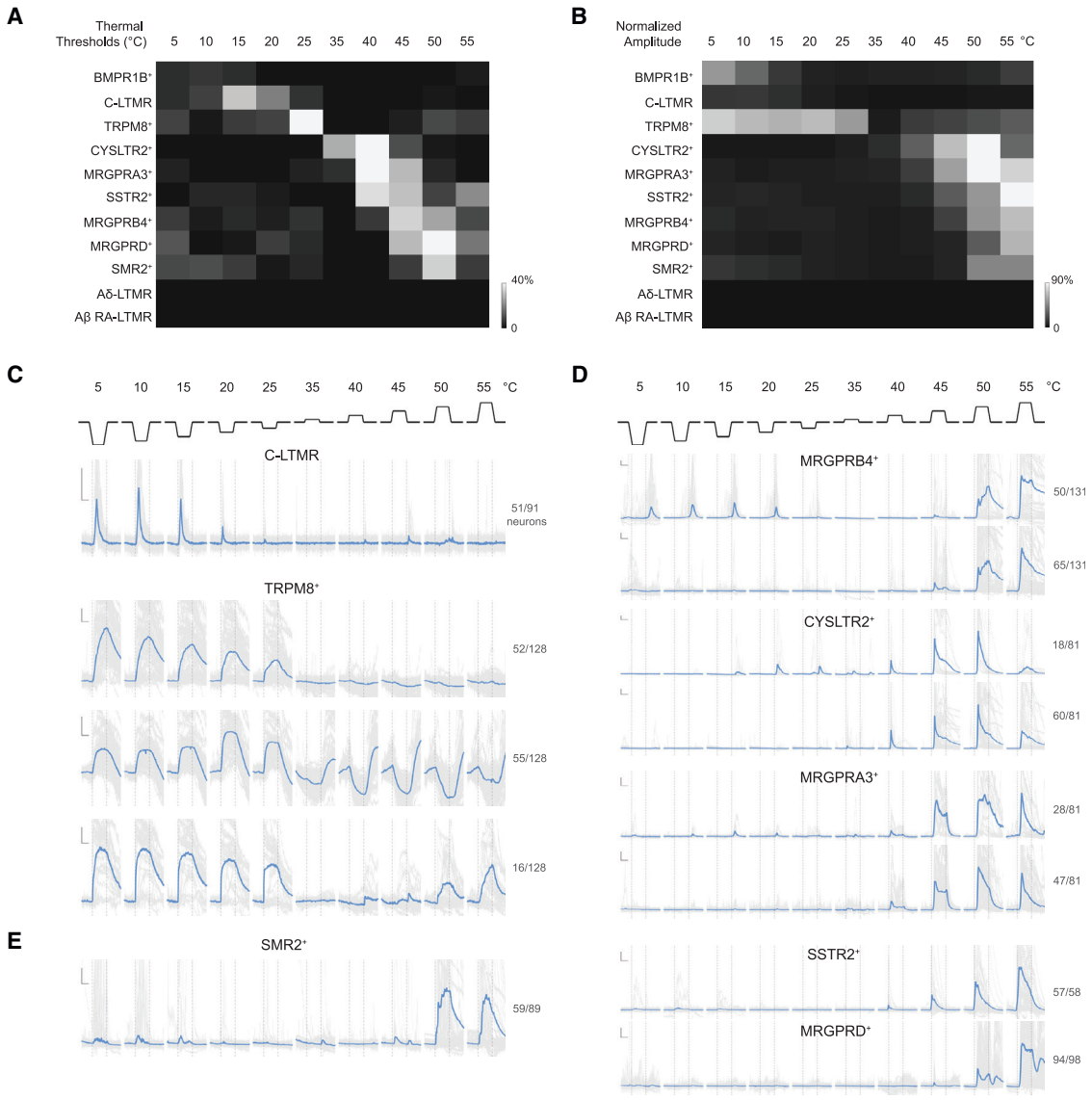

Figure 6. Temperature is reported as absolute or relative by distinct sensory neuron subtypes

(A) Summary of thermal thresholds for DRG neuron subtypes, with percentage at each threshold indicated by the brightness level. Aβ RA-LTMRs and Aδ-LTMRs were set to zero due to lack of thermal responses.

(B) Summary of response amplitudes (ΔF/F) for DRG neuron subtypes, normalized to each neuron's maximum response to all stimuli, and averaged within each subtype.

(C) Diverse response profiles to cooling. C-LTMRs exhibited transient responses to temperature decrease. TRPM8$^+$ neurons showed three types of responses: cooling activated (top), cooling activated and warmth inhibited (middle), and cooling-and-heat activated (bottom).

(D) Diverse response profiles to warmth or heat. MRGPRB4$^+$, CYSLTR2$^+$, and MRGPRA3$^+$ neurons exhibited two types of responses: neurons responding to relative increase (top) and only to absolute temperature (bottom). SSTR2$^+$ and MRGPRD$^+$ neurons responded to absolute warmth/heat.

(E) SMR2$^+$ neurons exhibit responses to heat and/or cold.

Scale bars in (C)–(E): 20% ΔF/F (y axis), 10 s (x axis). Individual traces are shown in gray and the average trace in blue. Dashed vertical lines mark temperature change. From (C)–(E), neuron counts (plotted/total imaged) are provided in the right.

for labeling transcriptionally distinct DRG neuron subtypes. We used this resource to reveal a remarkable degree of morphological and physiological diversity across the transcriptionally distinct DRG neuron subtypes. This mouse DRG neuron toolkit should enable analyses of the neuronal building blocks of somatosensation.

Genetic access to the principal DRG neuron subtypes

Transcriptomic analyses, including measurements reported herein, have revealed more than 15 transcriptionally distinct DRG neuron populations. These transcriptomic data were used to generate and curate a collection of genetic tools for the major DRG neuron populations. Genetic access to several DRG neuron

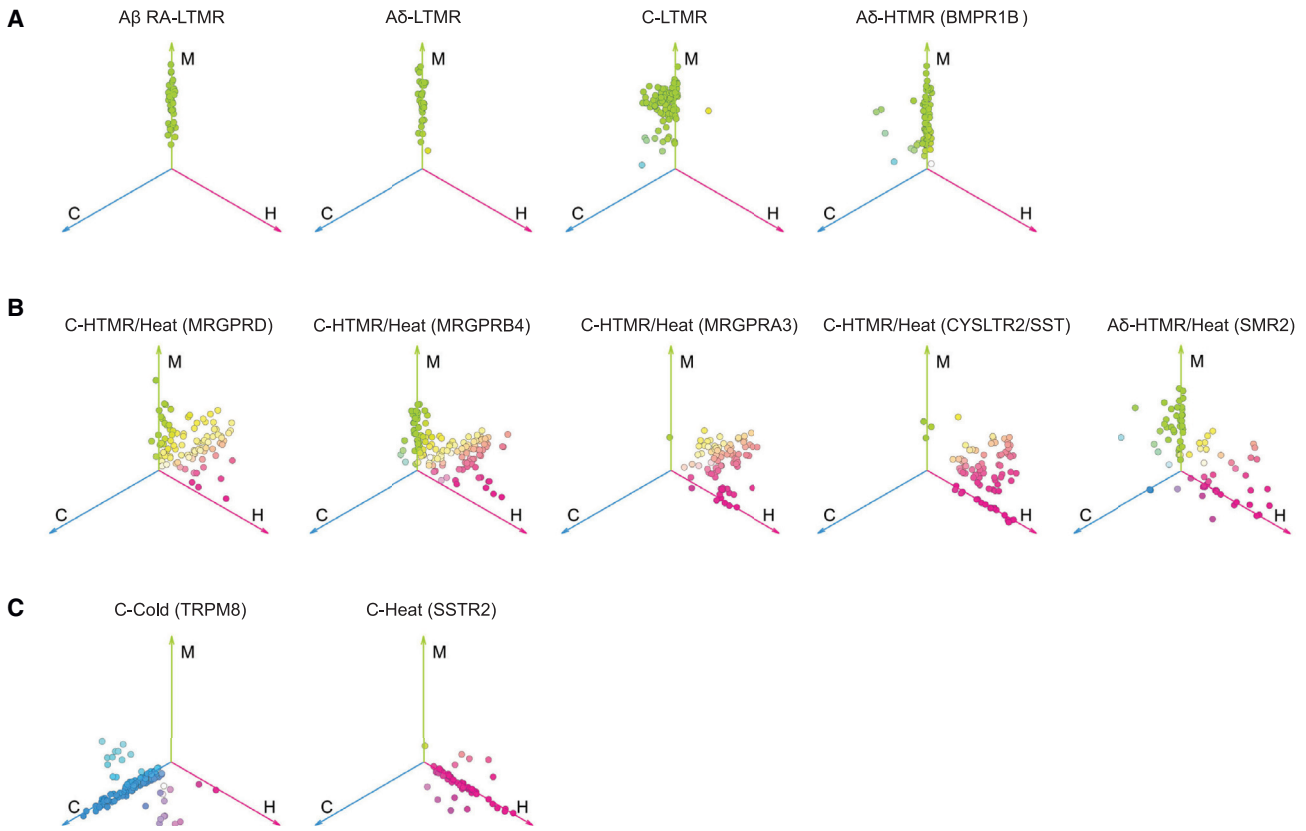

Figure 7. Polymodality of DRG neuron subtypes

Distributions of tuning preferences for each DRG subtype. Each neuron is represented by a dot, positioned based on its maximum response magnitude to mechanical (M), heat (H), or cold (C) stimuli. Dot color shows relative preference for these modalities, with white dots near the center indicating tuning to all three. Subtypes exhibiting strong preference to mechanical stimuli are in (A), those with polymodal responses in (B), and those primarily responding to thermal stimuli in (C).

See also Figure S7.

classes or subtypes, including C-LTMRs, Aδ-LTMRs, Aβ RA-LTMRs, Aβ field-LTMRs, Aβ SA-LTMRs, and the broad proprioceptor population, had been previously achieved[15–17,19,27,30,54] and further confirmed using the functional analyses in this study. In contrast, although CGRP$^+$ DRG neurons have been recognized as physiologically and morphologically heterogeneous,[22,40,56] subpopulations of this important class of sensory neurons were lacking genetic tools and, consequently, discerning the properties and functions of C-fiber and Aδ-fiber CGRP$^+$ neuron subtypes had been a challenge. Resolving the morphological and physiological diversity of CGRP$^+$ neuron subtypes is of great interest because, as a collective, they are implicated in nociception.[22,81] Genetic tools generated for accessing CGRP$^+$ neuronal subtypes, described here, have enabled insights into their properties and functions. For example, CGRP$^+$ epidermal-penetrating FNEs comprise intermingled endings of Aδ-HTMR/Heat (SMR2) neurons and C-Heat (SSTR2) neurons. Furthermore, although each cutaneous DRG neuron subtype appears to fully innervate most or all areas of hairy skin across the body, our sparse labeling studies suggest that FNE subtypes often exhibited a degree of homotypic overlap of their cutaneous axons (Figures S4A and S4C). This latter observation contrasts with the high degree of homotypic tiling observed for several LTMR subtypes.[18,82]

It is noteworthy that scRNA-seq of human DRG neurons revealed that human DRGs contain subtypes that, on a transcriptome-wide level, resemble DRG subtypes described in mouse, although individual genes within subtypes can vary between mouse and human.[37,83–86]

Molecular basis of DRG neuron response properties

To relate the molecular basis of sensory reactivity to the observed physiological response properties across the DRG neuron subtypes, we compared the mRNA abundance of mechanically and thermally activated ion channels in the neuronal subtypes using the single-cell transcriptomic dataset (Figure S7). It is notable that all LTMR and HTMR subtypes exhibit moderate to high levels of Piezo2 expression,[34,87–90] whereas mechano-insensitive subtypes, the C-Heat (SSTR2) and C-Cold (TRPM8) populations, exhibit trace expression of Piezo2. Interestingly, we also observed that HTMR subtypes with denser branching patterns (e.g., C-HTMR/Heat [MRGPRD] neurons) had lower force thresholds compared with those with a sparse branching pattern (e.g., Aδ-HTMR/Heat [SMR2] neurons) (Figures 2G and

4C). Therefore, it is tempting to speculate that denser branching patterns could increase the probability of receptor potential summation following focal indentation, thereby decreasing the amount of force needed for action potential generation. Additional determinants of mechano-responsivity include the axonal structures and other cellular constituents of mechanosensory end organs,[1,91] ion channels underlying intrinsic excitability,[40] modulation by non-neuronal cells,[70,92–97] expression of Piezo1,[98] and other potential mechano-sensitive molecules and auxiliary proteins.[99–102]

By contrast, thermosensitivity may be explained, in part, by combinations of TRP channels in transcriptionally distinct DRG neuron subtypes. The warm-sensitive neuronal subtypes, with thermal thresholds in the 35°C–40°C range, including C-HTMR/Heat (CYSLTR2/SST), C-HTMR/Heat (MRGPRA3), and C-Heat (SSTR2) neurons, express high levels of TRPV1 (Figure S7B), which contributes to warmth encoding.[65,103–105] C-HTMR/Heat (CYSLTR2/SST) neurons also express TRPM2 (Figure S7), another warm-sensing molecule.[106] We note that the Oprk1^{+} population also expresses TRPV1, and we suspect that these neurons also contribute to warm encoding, although testing this prediction must await functional analysis of this population. Additionally, TRPM3, TRPV2 and TRPA1 are expressed in both C-HTMR/Heat (MRGPRD) and C-HTMR/Heat (MRGPRB4) neurons (Figure S7), potentially contributing to their thermal sensitivity.[107–109] C-Cold (TRPM8) neurons uniquely express high levels of TRPM8,[52,53,64,110] and a subset also expresses TRPV1 (Figure S7B), which we speculate explains the heat sensitivity of some C-Cold (TRPM8) neurons (Figure 6C). Curiously, C-LTMRs do not express detectable levels of known thermal TRP channels; therefore, how these neurons respond to cooling the skin remains unclear. Thus, the diverse thermal response dynamics and the encoding of temperature (Figures 6C and 6D) likely involve mechanisms beyond those employing TRP channels expressed in DRG neurons.[111–113]

Sensory neurons are also responsive to a range of chemicals. Given the extensive studies on activation of TRP channels by natural products,[8] it is possible to predict responses of distinct DRG populations to compounds, such as capsaicin, by assessing their expression of TRP channels (Figure S7B). Similarly, expression of receptors for pruritogens and inflammatory mediators of pain can also be assessed across the subtypes[11,114] (Figure S7C). The abundant expression of itch receptors in C-HTMR/Heat (MRGPRA3) and C-HTMR/Heat (CYSLTR2/SST) subtypes underscores their important roles in pruriception, whereas expression patterns of receptors for inflammatory mediators provide insights into subtypes involved in inflammatory pain. These data should help delineate chemical sensitivity across the DRG neuron populations.

DRG neuron types and the tiling of mechanical and thermal stimulus space

By systematically comparing indentation force thresholds of DRG neurons, we found a graded distribution of thresholds across the subtypes (Figure 4C). Moreover, although LTMR subtype responses saturated in innocuous force ranges, at least five of the HTMR subtypes displayed clear activation by innocuous forces and maximum activation with noxious forces, such as pinch (Figures 4D, 5C, and 5D). Therefore, although HTMR subtypes are often considered under the nociceptor umbrella, we propose that this nomenclature is not ideal because it does not take into account the broad range of responsiveness of most HTMR subtypes, particularly in the innocuous force range. The classical use of the term nociceptor refers to a neuron that encodes stimulus intensity into the noxious range, regardless of whether it exhibits spiking at lower, innocuous force presentations.[3] Additionally, emerging evidence indicates that activation of certain HTMRs does not necessarily lead to pain perception or a nocifensive response.[2,79,115] For example, microneurography recordings in conscious human subjects revealed that mechanically evoked C-HTMR/Heat fibers can discharge up to 10 Hz without an accompanying painful percept.[116] Moreover, recent work in mice has indicated that optogenetic activation of C-HTMR/Heat (MRGPRD) neurons, did not lead to place aversion in a place preference test[79] or trigger a "pain-like" behavior evaluated using a mouse pain scale.[115] Furthermore, activation of C-HTMR/Heat (MRGPRB4) neurons does not evoke nocifensive behaviors.[29,68] These considerations support the view that most HTMR subtypes are poised to contribute to the encoding of innocuous forces acting on the skin, rather than solely contributing to pain. We do note that the Aδ-HTMR/Heat (SMR2) population represents an exception to this heuristic. The Aδ-HTMR/Heat (SMR2) neurons are activated exclusively by noxious mechanical stimuli, exhibiting little to no activation in the innocuous stimulus range (Figures 4C, 4D, and 5A–5D); therefore, this population appears to exclusively encode noxious stimuli.

Related to this, several DRG neuron subtypes have been implicated in chemical signaling, and some of these subtypes have been designated as pruriceptors (itch receptors). Indeed, activation of C-HTMR/Heat (CYSLTR2/SST) or C-HTMR/Heat (MRGPRA3) neurons can evoke scratching behaviors,[10,11,25,31,69,98,117] and these subtypes express distinct receptors for chemical stimuli (Figure S7C),[60,61,118–122] rendering them sensitive to compounds capable of eliciting the perception of itch. It follows that chemical stimuli activate combinations of somatosensory neuron subtypes distinct from the ensembles activated by mechanical or thermal stimuli. It is therefore likely that different percepts arise when distinct combinations of DRG neuron subtypes are co-activated. In support of this idea, the "pruriceptor" populations, C-HTMR/Heat (CYSLTR2/SST) and C-HTMR/Heat (MRGPRA3) neurons, are activated by indenting or warming of the skin, which do not necessarily evoke scratching behaviors. We therefore favor the view that a behavioral response or a particular percept arises from the combinatorial nature of the cohort of subtypes activated by a given stimulus, the convergence and integration of these signals in the spinal cord and brainstem, and the subsequent neural computations made by these higher-order circuits.[7,123,124] These deductions lead us to encourage the use of a taxonomy of primary somatosensory neurons that is based on physiological properties rather than specific percepts or behaviors, such as those implied by the terms nociceptor or pruriceptor.

In sum, our findings indicate that at least 12 morphologically, physiologically, and transcriptionally distinct DRG neuron subtypes encode mechanical forces (at least six LTMRs, the responses of two of these—Aβ field-LTMRs and Pacinian

corpuscle/Aβ RA2-LTMRs—were not studied here, and at least six HTMRs) and no fewer than eight distinct subtypes encode thermal stimuli acting on the skin, with six exhibiting polymodality. Interestingly, mechanical force space is tiled by indentation force thresholds of the LTMR and HTMR subtypes. In parallel with this, each of the thermally responsive DRG neuron subtypes encodes thermal stimuli within a distinct temperature range; therefore, thermal space is also tiled by the response thresholds of thermally responsive neuron subtypes. Thus, distinct cohorts of DRG neuron subtypes are recruited as the force of indentation increases or as the temperature of a thermal stimulus increases or decreases. This general inference may hold true across other "dimensions" of somatosensation. For example, for vibration tuning, low (1–10 Hz), medium (10–200 Hz), and high (200–1,000 Hz) frequency vibrations of the skin are encoded by different mechanoreceptor subtypes.[1] Therefore, the somatosensory system is composed of physiologically distinct primary sensory neuron subtypes with distinct activation patterns for thermal, mechanical, or chemical stimuli; thus, a combination of population and rate codes signifies where within a particular dimensional space a stimulus resides.

Limitations of the study

Future studies will be required to gain selective genetic access to at least one transcriptionally distinct CGRP$^+$ DRG neuron subtype (Oprk1$^+$ neurons), as well as, but not limited to, neurons that innervate Pacinian corpuscles. Moreover, our study focused on hairy skin; future studies are required to compare response properties of subtypes that innervate other skin regions and visceral organs and under pathological conditions.[23,39,65,79,87,125–127] Also, it is likely that there exist additional DRG neuron subtypes that were either too rare or labile to detect by the transcriptomic approaches used in the present study.

STAR★METHODS

Detailed methods are provided in the online version of this paper and include the following:

- KEY RESOURCES TABLE
- RESOURCE AVAILABILITY
  - Lead contact
  - Materials availability
  - Data and code availability
- EXPERIMENTAL MODELS AND STUDY PARTICIPANT DETAILS
  - Mouse lines
  - Genotyping
  - Tamoxifen treatment
- METHOD DETAILS
  - Single-cell RNA-seq
  - scRNA-seq analysis
  - AAV production and neonatal IP injection
  - Immunohistochemistry
  - Quantification of spinal cord terminals
  - *In situ* hybridization (RNAscope)
  - Sparse labeling for single-neuron morphological analysis
  - Whole-mount alkaline phosphatase staining of the skin and spinal cord
  - Quantification of skin arborizations in the sparse labeling experiments
  - Axial level analysis of *Adra2a*$^{T2a\text{-}CreER}$ labeling
  - *In vivo* epifluorescence calcium imaging
  - Stimuli applications
  - Calcium Imaging analysis
- QUANTIFICATION AND STATISTICAL ANALYSIS

SUPPLEMENTAL INFORMATION

Supplemental information can be found online at https://doi.org/10.1016/j.cell.2024.02.006.

ACKNOWLEDGMENTS

We thank O. Mazor and P. Gorelik (HMS Research Instrumentation Core) for help with design and construction of the GCaMP imaging setup and stimulation devices and Ginty lab and Sharma lab members for discussions and comments on the manuscript. We thank Caiying Guo at Janelia Research Campus for generating mouse lines. This work was supported by a Quan Predoctoral Fellowship (L.Q.), NIH grants NS097344 (D.D.G.), AT011447 (D.D.G.), and 1DP2NS127278 (N.S.), The Klingenstein-Simons Foundation (N.S.), The Whitehall Foundation (N.S.), The Bertarelli Foundation (D.D.G.), The Hock E. Tan and Lisa Yang Center for Autism Research (D.D.G.), and the Lefler Center for Neurodegenerative Disorders (D.D.G.). D.D.G. is an HHMI investigator. This article is subject to HHMI's open access to publications policy. HHMI lab heads have previously granted a nonexclusive CC BY 4.0 license to the public and a sublicensable license to HHMI in their research articles. Pursuant to those licenses, the author-accepted manuscript of this article can be made freely available under a CC BY 4.0 license immediately upon publication.

AUTHOR CONTRIBUTIONS

N.S., L.Q., and D.D.G. conceived the study. N.S. and D.D.G. designed the mouse lines generated in this study, except for *Cysltr2*$^{T2A\text{-}Cre}$, which was generated by T.V., M.P., V.K.K., and I.C. L.Q., N.S., and M.I. characterized the mouse lines and performed all histological and morphological analyses with help from D.S., C.W., K.L., and P.R. L.Q. performed the GCaMP imaging experiments, with help from N.S. N.S., L.Q., and D.D.G. wrote the paper with input from all authors.

DECLARATION OF INTERESTS

The authors declare no competing interests.

Received: April 22, 2023
Revised: November 12, 2023
Accepted: February 5, 2024
Published: March 4, 2024

REFERENCES

1. Handler, A., and Ginty, D.D. (2021). The mechanosensory neurons of touch and their mechanisms of activation. Nat. Rev. Neurosci. *22*, 521–537.
2. Dubin, A.E., and Patapoutian, A. (2010). Nociceptors: the sensors of the pain pathway. J. Clin. Invest. *120*, 3760–3772.
3. Bessou, P., and Perl, E.R. (1969). Response of cutaneous sensory units with unmyelinated fibers to noxious stimuli. J. Neurophysiol. *32*, 1025–1043.

4. Lewin, G.R., and Moshourab, R. (2004). Mechanosensation and pain. J. Neurobiol. *61*, 30–44.

5. Smith, E.S., and Lewin, G.R. (2009). Nociceptors: a phylogenetic view. J. Comp. Physiol. A Neuroethol. Sens. Neural Behav. Physiol. *195*, 1089–1106.

6. Schepers, R.J., and Ringkamp, M. (2009). Thermoreceptors and thermosensitive afferents. Neurosci. Biobehav. Rev. *33*, 205–212.

7. LaMotte, R.H., Dong, X., and Ringkamp, M. (2014). Sensory neurons and circuits mediating itch. Nat. Rev. Neurosci. *15*, 19–31.

8. Julius, D. (2013). TRP channels and pain. Annu. Rev. Cell Dev. Biol. *29*, 355–384.

9. Basbaum, A.I., Bautista, D.M., Scherrer, G., and Julius, D. (2009). Cellular and molecular mechanisms of pain. Cell *139*, 267–284.

10. Bautista, D.M., Wilson, S.R., and Hoon, M.A. (2014). Why we scratch an itch: the molecules, cells and circuits of itch. Nat. Neurosci. *17*, 175–182.

11. Lay, M., and Dong, X. (2020). Neural Mechanisms of Itch. Annu. Rev. Neurosci. *43*, 187–205.

12. Grundy, L., Erickson, A., and Brierley, S.M. (2019). Visceral Pain. Annu. Rev. Physiol. *81*, 261–284.

13. Cervero, F. (1994). Sensory innervation of the viscera: peripheral basis of visceral pain. Physiol. Rev. *74*, 95–138.

14. Chen, H.H., Hippenmeyer, S., Arber, S., and Frank, E. (2003). Development of the monosynaptic stretch reflex circuit. Curr. Opin. Neurobiol. *13*, 96–102.

15. Bai, L., Lehnert, B.P., Liu, J., Neubarth, N.L., Dickendesher, T.L., Nwe, P.H., Cassidy, C., Woodbury, C.J., and Ginty, D.D. (2015). Genetic Identification of an Expansive Mechanoreceptor Sensitive to Skin Stroking. Cell *163*, 1783–1795.

16. Li, L., Rutlin, M., Abraira, V.E., Cassidy, C., Kus, L., Gong, S., Jankowski, M.P., Luo, W., Heintz, N., Koerber, H.R., et al. (2011). The functional organization of cutaneous low-threshold mechanosensory neurons. Cell *147*, 1615–1627.

17. Luo, W., Enomoto, H., Rice, F.L., Milbrandt, J., and Ginty, D.D. (2009). Molecular identification of rapidly adapting mechanoreceptors and their developmental dependence on ret signaling. Neuron *64*, 841–856.

18. Neubarth, N.L., Emanuel, A.J., Liu, Y., Springel, M.W., Handler, A., Zhang, Q., Lehnert, B.P., Guo, C., Orefice, L.L., Abdelaziz, A., et al. (2020). Meissner corpuscles and their spatially intermingled afferents underlie gentle touch perception. Science *368*, eabb2751.

19. Rutlin, M., Ho, C.Y., Abraira, V.E., Cassidy, C., Bai, L., Woodbury, C.J., and Ginty, D.D. (2014). The cellular and molecular basis of direction selectivity of Adelta-LTMRs. Cell *159*, 1640–1651.

20. Liu, Q., Vrontou, S., Rice, F.L., Zylka, M.J., Dong, X., and Anderson, D.J. (2007). Molecular genetic visualization of a rare subset of unmyelinated sensory neurons that may detect gentle touch. Nat. Neurosci. *10*, 946–948.

21. Zylka, M.J., Rice, F.L., and Anderson, D.J. (2005). Topographically distinct epidermal nociceptive circuits revealed by axonal tracers targeted to Mrgprd. Neuron *45*, 17–25.

22. Ghitani, N., Barik, A., Szczot, M., Thompson, J.H., Li, C., Le Pichon, C.E., Krashes, M.J., and Chesler, A.T. (2017). Specialized Mechanosensory Nociceptors Mediating Rapid Responses to Hair Pull. Neuron *95*, 944–954.e4.

23. Prato, V., Taberner, F.J., Hockley, J.R.F., Callejo, G., Arcourt, A., Tazir, B., Hammer, L., Schad, P., Heppenstall, P.A., Smith, E.S., and Lechner, S.G. (2017). Functional and Molecular Characterization of Mechanoinsensitive "Silent" Nociceptors. Cell Rep. *21*, 3102–3115.

24. Snyder, L.M., Chiang, M.C., Loeza-Alcocer, E., Omori, Y., Hachisuka, J., Sheahan, T.D., Gale, J.R., Adelman, P.C., Sypek, E.I., Fulton, S.A., et al. (2018). Kappa Opioid Receptor Distribution and Function in Primary Afferents. Neuron *99*, 1274–1288.e6.

25. Han, L., Ma, C., Liu, Q., Weng, H.J., Cui, Y., Tang, Z., Kim, Y., Nie, H., Qu, L., Patel, K.N., et al. (2013). A subpopulation of nociceptors specifically linked to itch. Nat. Neurosci. *16*, 174–182.

26. Arcourt, A., Gorham, L., Dhandapani, R., Prato, V., Taberner, F.J., Wende, H., Gangadharan, V., Birchmeier, C., Heppenstall, P.A., and Lechner, S.G. (2017). Touch Receptor-Derived Sensory Information Alleviates Acute Pain Signaling and Fine-Tunes Nociceptive Reflex Coordination. Neuron *93*, 179–193.

27. Abraira, V.E., Kuehn, E.D., Chirila, A.M., Springel, M.W., Toliver, A.A., Zimmerman, A.L., Orefice, L.L., Boyle, K.A., Bai, L., Song, B.J., et al. (2017). The Cellular and Synaptic Architecture of the Mechanosensory Dorsal Horn. Cell *168*, 295–310.e19.

28. Sharma, N., Flaherty, K., Lezgiyeva, K., Wagner, D.E., Klein, A.M., and Ginty, D.D. (2020). The emergence of transcriptional identity in somatosensory neurons. Nature *577*, 392–398.

29. Vrontou, S., Wong, A.M., Rau, K.K., Koerber, H.R., and Anderson, D.J. (2013). Genetic identification of C fibres that detect massage-like stroking of hairy skin in vivo. Nature *493*, 669–673.

30. Olson, W., Abdus-Saboor, I., Cui, L., Burdge, J., Raabe, T., Ma, M., and Luo, W. (2017). Sparse genetic tracing reveals regionally specific functional organization of mammalian nociceptors. eLife *6*, e29507.

31. Huang, J., Polgár, E., Solinski, H.J., Mishra, S.K., Tseng, P.Y., Iwagaki, N., Boyle, K.A., Dickie, A.C., Kriegbaum, M.C., Wildner, H., et al. (2018). Circuit dissection of the role of somatostatin in itch and pain. Nat. Neurosci. *21*, 707–716.

32. Liu, S., Wang, Z., Su, Y., Qi, L., Yang, W., Fu, M., Jing, X., Wang, Y., and Ma, Q. (2021). A neuroanatomical basis for electroacupuncture to drive the vagal-adrenal axis. Nature *598*, 641–645.

33. Li, F., Jiang, H., Shen, X., Yang, W., Guo, C., Wang, Z., Xiao, M., Cui, L., Luo, W., Kim, B.S., et al. (2021). Sneezing reflex is mediated by a peptidergic pathway from nose to brainstem. Cell *184*, 3762–3773.e10.

34. von Buchholtz, L.J., Ghitani, N., Lam, R.M., Licholai, J.A., Chesler, A.T., and Ryba, N.J.P. (2021). Decoding Cellular Mechanisms for Mechanosensory Discrimination. Neuron *109*, 285–298.e5.

35. Zeisel, A., Hochgerner, H., Lönnerberg, P., Johnsson, A., Memic, F., van der Zwan, J., Häring, M., Braun, E., Borm, L.E., La Manno, G., et al. (2018). Molecular Architecture of the Mouse Nervous System. Cell *174*, 999–1014.e22.

36. Usoskin, D., Furlan, A., Islam, S., Abdo, H., Lönnerberg, P., Lou, D., Hjerling-Leffler, J., Haeggström, J., Kharchenko, O., Kharchenko, P.V., et al. (2015). Unbiased classification of sensory neuron types by large-scale single-cell RNA sequencing. Nat. Neurosci. *18*, 145–153.

37. Bhuiyan, S.A., Xu, M., Yang, L., Semizoglou, E., Bhatia, P., Pantaleo, K.I., Tochitsky, I., Jain, A., Erdogan, B., Blair, S., et al. (2023). Harmonized cross-species cell atlases of trigeminal and dorsal root ganglia. Preprint at bioRxiv. https://doi.org/10.1101/2023.07.04.547740.

38. Zhang, C., Hu, M.W., Wang, X.W., Cui, X., Liu, J., Huang, Q., Cao, X., Zhou, F.Q., Qian, J., He, S.Q., et al. (2022). scRNA-sequencing reveals subtype-specific transcriptomic perturbations in DRG neurons of Pirt(EGFPf) mice in neuropathic pain condition. eLife *11*, e76063.

39. Renthal, W., Tochitsky, I., Yang, L., Cheng, Y.C., Li, E., Kawaguchi, R., Geschwind, D.H., and Woolf, C.J. (2020). Transcriptional Reprogramming of Distinct Peripheral Sensory Neuron Subtypes after Axonal Injury. Neuron *108*, 128–144.e9.

40. Zheng, Y., Liu, P., Bai, L., Trimmer, J.S., Bean, B.P., and Ginty, D.D. (2019). Deep Sequencing of Somatosensory Neurons Reveals Molecular Determinants of Intrinsic Physiological Properties. Neuron *103*, 598–616.e7.

41. Li, C.L., Li, K.C., Wu, D., Chen, Y., Luo, H., Zhao, J.R., Wang, S.S., Sun, M.M., Lu, Y.J., Zhong, Y.Q., et al. (2016). Somatosensory neuron types identified by high-coverage single-cell RNA-sequencing and functional heterogeneity. Cell Res. *26*, 83–102.

42. Wende, H., Lechner, S.G., Cheret, C., Bourane, S., Kolanczyk, M.E., Pattyn, A., Reuter, K., Munier, F.L., Carroll, P., Lewin, G.R., and Birchmeier, C. (2012). The transcription factor c-Maf controls touch receptor development and function. Science *335*, 1373–1376.

43. Ichikawa, H., Deguchi, T., Nakago, T., Jacobowitz, D.M., and Sugimoto, T. (1994). Parvalbumin, calretinin and carbonic anhydrase in the trigeminal and spinal primary neurons of the rat. Brain Res. *655*, 241–245.

44. Kobayashi, K., Fukuoka, T., Obata, K., Yamanaka, H., Dai, Y., Tokunaga, A., and Noguchi, K. (2005). Distinct expression of TRPM8, TRPA1, and TRPV1 mRNAs in rat primary afferent neurons with adelta/c-fibers and colocalization with trk receptors. J. Comp. Neurol. *493*, 596–606.

45. Rosenfeld, M.G., Mermod, J.J., Amara, S.G., Swanson, L.W., Sawchenko, P.E., Rivier, J., Vale, W.W., and Evans, R.M. (1983). Production of a novel neuropeptide encoded by the calcitonin gene via tissue-specific RNA processing. Nature *304*, 129–135.

46. Dong, X., Han, S., Zylka, M.J., Simon, M.I., and Anderson, D.J. (2001). A diverse family of GPCRs expressed in specific subsets of nociceptive sensory neurons. Cell *106*, 619–632.

47. Zylka, M.J., Dong, X., Southwell, A.L., and Anderson, D.J. (2003). Atypical expansion in mice of the sensory neuron-specific Mrg G protein-coupled receptor family. Proc. Natl. Acad. Sci. USA *100*, 10043–10048.

48. Arber, S., Ladle, D.R., Lin, J.H., Frank, E., and Jessell, T.M. (2000). ETS gene Er81 controls the formation of functional connections between group Ia sensory afferents and motor neurons. Cell *101*, 485–498.

49. de Nooij, J.C., Doobar, S., and Jessell, T.M. (2013). Etv1 inactivation reveals proprioceptor subclasses that reflect the level of NT3 expression in muscle targets. Neuron *77*, 1055–1068.

50. Stantcheva, K.K., Iovino, L., Dhandapani, R., Martinez, C., Castaldi, L., Nocchi, L., Perlas, E., Portulano, C., Pesaresi, M., Shirlekar, K.S., et al. (2016). A subpopulation of itch-sensing neurons marked by Ret and somatostatin expression. EMBO Rep. *17*, 585–600.

51. Mishra, S.K., and Hoon, M.A. (2013). The cells and circuitry for itch responses in mice. Science *340*, 968–971.

52. Bautista, D.M., Siemens, J., Glazer, J.M., Tsuruda, P.R., Basbaum, A.I., Stucky, C.L., Jordt, S.E., and Julius, D. (2007). The menthol receptor TRPM8 is the principal detector of environmental cold. Nature *448*, 204–208.

53. McKemy, D.D., Neuhausser, W.M., and Julius, D. (2002). Identification of a cold receptor reveals a general role for TRP channels in thermosensation. Nature *416*, 52–58.

54. Hippenmeyer, S., Vrieseling, E., Sigrist, M., Portmann, T., Laengle, C., Ladle, D.R., and Arber, S. (2005). A developmental switch in the response of DRG neurons to ETS transcription factor signaling. PLoS Biol. *3*, e159.

55. Cowie, A.M., Moehring, F., O'Hara, C., and Stucky, C.L. (2018). Optogenetic Inhibition of CGRPalpha Sensory Neurons Reveals Their Distinct Roles in Neuropathic and Incisional Pain. J. Neurosci. *38*, 5807–5825.

56. McCoy, E.S., Taylor-Blake, B., and Zylka, M.J. (2012). CGRPalpha-expressing sensory neurons respond to stimuli that evoke sensations of pain and itch. PLoS One *7*, e36355.

57. Delfini, M.C., Mantilleri, A., Gaillard, S., Hao, J., Reynders, A., Malapert, P., Alonso, S., Francois, A., Barrere, C., Seal, R., and Landry, M. (2013). TAFA4, a chemokine-like protein, modulates injury-induced mechanical and chemical pain hypersensitivity in mice. Cell rep. *5*, 378–388.

58. Nguyen, M.Q., Wu, Y., Bonilla, L.S., von Buchholtz, L.J., and Ryba, N.J.P. (2017). Diversity amongst trigeminal neurons revealed by high throughput single cell sequencing. PLoS One *12*, e0185543.

59. Seal, R.P., Wang, X., Guan, Y., Raja, S.N., Woodbury, C.J., Basbaum, A.I., and Edwards, R.H. (2009). Injury-induced mechanical hypersensitivity requires C-low threshold mechanoreceptors. Nature *462*, 651–655.

60. Voisin, T., Perner, C., Messou, M.A., Shiers, S., Ualiyeva, S., Kanaoka, Y., Price, T.J., Sokol, C.L., Bankova, L.G., Austen, K.F., and Chiu, I.M. (2021). The CysLT(2)R receptor mediates leukotriene C(4)-driven acute and chronic itch. Proc. Natl. Acad. Sci. USA *118*, e2022087118.

61. Chiu, I.M., Barrett, L.B., Williams, E.K., Strochlic, D.E., Lee, S., Weyer, A.D., Lou, S., Bryman, G.S., Roberson, D.P., Ghasemlou, N., et al. (2014). Transcriptional profiling at whole population and single cell levels reveals somatosensory neuron molecular diversity. eLife *3*.

62. Taniguchi, H., He, M., Wu, P., Kim, S., Paik, R., Sugino, K., Kvitsiani, D., Fu, Y., Lu, J., Lin, Y., et al. (2011). A resource of Cre driver lines for genetic targeting of GABAergic neurons in cerebral cortex. Neuron *71*, 995–1013.

63. Takashima, Y., Daniels, R.L., Knowlton, W., Teng, J., Liman, E.R., and McKemy, D.D. (2007). Diversity in the neural circuitry of cold sensing revealed by genetic axonal labeling of transient receptor potential melastatin 8 neurons. J. Neurosci. *27*, 14147–14157.

64. Dhaka, A., Murray, A.N., Mathur, J., Earley, T.J., Petrus, M.J., and Patapoutian, A. (2007). TRPM8 is required for cold sensation in mice. Neuron *54*, 371–378.

65. Yarmolinsky, D.A., Peng, Y., Pogorzala, L.A., Rutlin, M., Hoon, M.A., and Zuker, C.S. (2016). Coding and Plasticity in the Mammalian Thermosensory System. Neuron *92*, 1079–1092.

66. Cai, X., Huang, H., Kuzirian, M.S., Snyder, L.M., Matsushita, M., Lee, M.C., Ferguson, C., Homanics, G.E., Barth, A.L., and Ross, S.E. (2016). Generation of a KOR-Cre knockin mouse strain to study cells involved in kappa opioid signaling. Genesis *54*, 29–37.

67. Wolfson, R.L., Abdelaziz, A., Rankin, G., Kushner, S., Qi, L., Mazor, O., Choi, S., Sharma, N., and Ginty, D.D. (2023). DRG afferents that mediate physiologic and pathologic mechanosensation from the distal colon. Cell *186*, 3368–3385.e18.

68. Elias, L.J., Succi, I.K., Schaffler, M.D., Foster, W., Gradwell, M.A., Bohic, M., Fushiki, A., Upadhyay, A., Ejoh, L.L., Schwark, R., et al. (2023). Touch neurons underlying dopaminergic pleasurable touch and sexual receptivity. Cell *186*, 577–590.e16. e516.

69. Cui, L., Guo, J., Cranfill, S.L., Gautam, M., Bhattarai, J., Olson, W., Beattie, K., Challis, R.C., Wu, Q., Song, X., et al. (2022). Glutamate in primary afferents is required for itch transmission. Neuron *110*, 809–823.e5.

70. Maksimovic, S., Nakatani, M., Baba, Y., Nelson, A.M., Marshall, K.L., Wellnitz, S.A., Firozi, P., Woo, S.H., Ranade, S., Patapoutian, A., and Lumpkin, E.A. (2014). Epidermal Merkel cells are mechanosensory cells that tune mammalian touch receptors. Nature *509*, 617–621.

71. Xing, Y., Steele, H.R., Hilley, H.B., Zhu, Y., Lawson, K., Niehoff, T., and Han, L. (2021). Visualizing the Itch-Sensing Skin Arbors. J. Invest. Dermatol. *141*, 1308–1316.

72. Dhaka, A., Earley, T.J., Watson, J., and Patapoutian, A. (2008). Visualizing cold spots: TRPM8-expressing sensory neurons and their projections. J. Neurosci. *28*, 566–575.

73. Abraira, V.E., and Ginty, D.D. (2013). The sensory neurons of touch. Neuron *79*, 618–639.

74. Iggo, A. (1960). Cutaneous mechanoreceptors with afferent C fibres. J. Physiol. *152*, 337–353.

75. Paricio-Montesinos, R., Schwaller, F., Udhayachandran, A., Rau, F., Walcher, J., Evangelista, R., Vriens, J., Voets, T., Poulet, J.F.A., and Lewin, G.R. (2020). The Sensory Coding of Warm Perception. Neuron *106*, 830–841.e3.

76. Warwick, C., Salsovic, J., Hachisuka, J., Smith, K.M., Sheahan, T.D., Chen, H., Ibinson, J., Koerber, H.R., and Ross, S.E. (2022). Cell type-specific calcium imaging of central sensitization in mouse dorsal horn. Nat. Commun. *13*, 5199.

77. Liu, Q., Sikand, P., Ma, C., Tang, Z., Han, L., Li, Z., Sun, S., LaMotte, R.H., and Dong, X. (2012). Mechanisms of itch evoked by beta-alanine. J. Neurosci. *32*, 14532–14537.

78. Rau, K.K., McIlwrath, S.L., Wang, H., Lawson, J.J., Jankowski, M.P., Zylka, M.J., Anderson, D.J., and Koerber, H.R. (2009). Mrgprd enhances excitability in specific populations of cutaneous murine polymodal nociceptors. J. Neurosci. *29*, 8612–8619.

79. Warwick, C., Cassidy, C., Hachisuka, J., Wright, M.C., Baumbauer, K.M., Adelman, P.C., Lee, K.H., Smith, K.M., Sheahan, T.D., Ross, S.E., and

Koerber, H.R. (2021). MrgprdCre lineage neurons mediate optogenetic allodynia through an emergent polysynaptic circuit. Pain *162*, 2120–2131.

80. Zeng, H. (2022). What is a cell type and how to define it? Cell *185*, 2739–2755.
81. McCoy, E.S., Taylor-Blake, B., Street, S.E., Pribisko, A.L., Zheng, J., and Zylka, M.J. (2013). Peptidergic CGRPalpha primary sensory neurons encode heat and itch and tonically suppress sensitivity to cold. Neuron *78*, 138–151.
82. Kuehn, E.D., Meltzer, S., Abraira, V.E., Ho, C.Y., and Ginty, D.D. (2019). Tiling and somatotopic alignment of mammalian low-threshold mechanoreceptors. Proc. Natl. Acad. Sci. USA *116*, 9168–9177.
83. Yu, H., Usoskin, D., Nagi, S.S., Hu, Y., Kupari, J., Bouchatta, O., Cranfill, S.L., Gautam, M., Su, Y., Lu, Y., et al. (2023). Single-Soma Deep RNA Sequencing of Human Dorsal Root Ganglion Neurons Reveals Novel Molecular and Cellular Mechanisms Underlying Somatosensation. Preprint at bioRxiv. https://doi.org/10.1101/2023.03.17.533207.
84. Jung, M., Dourado, M., Maksymetz, J., Jacobson, A., Laufer, B.I., Baca, M., Foreman, O., Hackos, D.H., Riol-Blanco, L., and Kaminker, J.S. (2023). Cross-species transcriptomic atlas of dorsal root ganglia reveals species-specific programs for sensory function. Nat. Commun. *14*, 366.
85. Tavares-Ferreira, D., Shiers, S., Ray, P.R., Wangzhou, A., Jeevakumar, V., Sankaranarayanan, I., Cervantes, A.M., Reese, J.C., Chamessian, A., Copits, B.A., et al. (2022). Spatial transcriptomics of dorsal root ganglia identifies molecular signatures of human nociceptors. Sci. Transl. Med. *14*, eabj8186.
86. Nguyen, M.Q., von Buchholtz, L.J., Reker, A.N., Ryba, N.J., and Davidson, S. (2021). Single-nucleus transcriptomic analysis of human dorsal root ganglion neurons. eLife *10*, e71752.
87. Szczot, M., Liljencrantz, J., Ghitani, N., Barik, A., Lam, R., Thompson, J.H., Bharucha-Goebel, D., Saade, D., Necaise, A., Donkervoort, S., et al. (2018). PIEZO2 mediates injury-induced tactile pain in mice and humans. Sci. Transl. Med. *10*, eaat9892.
88. Coste, B., Mathur, J., Schmidt, M., Earley, T.J., Ranade, S., Petrus, M.J., Dubin, A.E., and Patapoutian, A. (2010). Piezo1 and Piezo2 are essential components of distinct mechanically activated cation channels. Science *330*, 55–60.
89. Ranade, S.S., Woo, S.H., Dubin, A.E., Moshourab, R.A., Wetzel, C., Petrus, M., Mathur, J., Bégay, V., Coste, B., Mainquist, J., et al. (2014). Piezo2 is the major transducer of mechanical forces for touch sensation in mice. Nature *516*, 121–125.
90. Hill, R.Z., and Bautista, D.M. (2020). Getting in Touch with Mechanical Pain Mechanisms. Trends Neurosci. *43*, 311–325.
91. Handler, A., Zhang, Q., Pang, S., Nguyen, T.M., Iskols, M., Nolan-Tamariz, M., Cattel, S., Plumb, R., Sanchez, B., Ashjian, K., et al. (2023). Three-dimensional reconstructions of mechanosensory end organs suggest a unifying mechanism underlying dynamic, light touch. Neuron *111*, 3211–3229.e9.
92. Mikesell, A.R., Isaeva, O., Moehring, F., Sadler, K.E., Menzel, A.D., and Stucky, C.L. (2022). Keratinocyte PIEZO1 modulates cutaneous mechanosensation. eLife *11*, e65987.
93. Woo, S.H., Ranade, S., Weyer, A.D., Dubin, A.E., Baba, Y., Qiu, Z., Petrus, M., Miyamoto, T., Reddy, K., Lumpkin, E.A., et al. (2014). Piezo2 is required for Merkel-cell mechanotransduction. Nature *509*, 622–626.
94. Hoffman, B.U., Baba, Y., Griffith, T.N., Mosharov, E.V., Woo, S.H., Roybal, D.D., Karsenty, G., Patapoutian, A., Sulzer, D., and Lumpkin, E.A. (2018). Merkel Cells Activate Sensory Neural Pathways through Adrenergic Synapses. Neuron *100*, 1401–1413.e6.
95. Moehring, F., Cowie, A.M., Menzel, A.D., Weyer, A.D., Grzybowski, M., Arzua, T., Geurts, A.M., Palygin, O., and Stucky, C.L. (2018). Keratinocytes mediate innocuous and noxious touch via ATP-P2X4 signaling. eLife *7*, e31684.
96. Maricich, S.M., Wellnitz, S.A., Nelson, A.M., Lesniak, D.R., Gerling, G.J., Lumpkin, E.A., and Zoghbi, H.Y. (2009). Merkel cells are essential for light-touch responses. Science *324*, 1580–1582.
97. Baumbauer, K.M., DeBerry, J.J., Adelman, P.C., Miller, R.H., Hachisuka, J., Lee, K.H., Ross, S.E., Koerber, H.R., Davis, B.M., and Albers, K.M. (2015). Keratinocytes can modulate and directly initiate nociceptive responses. eLife *4*, e09674.
98. Hill, R.Z., Loud, M.C., Dubin, A.E., Peet, B., and Patapoutian, A. (2022). PIEZO1 transduces mechanical itch in mice. Nature *607*, 104–110.
99. Ranade, S.S., Syeda, R., and Patapoutian, A. (2015). Mechanically Activated Ion Channels. Neuron *87*, 1162–1179.
100. Schwaller, F., Bégay, V., García-García, G., Taberner, F.J., Moshourab, R., McDonald, B., Docter, T., Kühnemund, J., Ojeda-Alonso, J., Paricio-Montesinos, R., et al. (2021). USH2A is a Meissner's corpuscle protein necessary for normal vibration sensing in mice and humans. Nat. Neurosci. *24*, 74–81.
101. Poole, K., Herget, R., Lapatsina, L., Ngo, H.D., and Lewin, G.R. (2014). Tuning Piezo ion channels to detect molecular-scale movements relevant for fine touch. Nat. Commun. *5*, 3520.
102. Moehring, F., Halder, P., Seal, R.P., and Stucky, C.L. (2018). Uncovering the Cells and Circuits of Touch in Normal and Pathological Settings. Neuron *100*, 349–360.
103. Ran, C., Hoon, M.A., and Chen, X. (2016). The coding of cutaneous temperature in the spinal cord. Nat. Neurosci. *19*, 1201–1209.
104. Caterina, M.J., Leffler, A., Malmberg, A.B., Martin, W.J., Trafton, J., Petersen-Zeitz, K.R., Koltzenburg, M., Basbaum, A.I., and Julius, D. (2000). Impaired nociception and pain sensation in mice lacking the capsaicin receptor. Science *288*, 306–313.
105. Caterina, M.J., Schumacher, M.A., Tominaga, M., Rosen, T.A., Levine, J.D., and Julius, D. (1997). The capsaicin receptor: a heat-activated ion channel in the pain pathway. Nature *389*, 816–824.
106. Tan, C.H., and McNaughton, P.A. (2016). The TRPM2 ion channel is required for sensitivity to warmth. Nature *536*, 460–463.
107. Vriens, J., Owsianik, G., Hofmann, T., Philipp, S.E., Stab, J., Chen, X., Benoit, M., Xue, F., Janssens, A., Kerselaers, S., et al. (2011). TRPM3 is a nociceptor channel involved in the detection of noxious heat. Neuron *70*, 482–494.
108. Vandewauw, I., De Clercq, K., Mulier, M., Held, K., Pinto, S., Van Ranst, N., Segal, A., Voet, T., Vennekens, R., Zimmermann, K., et al. (2018). A TRP channel trio mediates acute noxious heat sensing. Nature *555*, 662–666.
109. Caterina, M.J., Rosen, T.A., Tominaga, M., Brake, A.J., and Julius, D. (1999). A capsaicin-receptor homologue with a high threshold for noxious heat. Nature *398*, 436–441.
110. Peier, A.M., Moqrich, A., Hergarden, A.C., Reeve, A.J., Andersson, D.A., Story, G.M., Earley, T.J., Dragoni, I., McIntyre, P., Bevan, S., and Patapoutian, A. (2002). A TRP channel that senses cold stimuli and menthol. Cell *108*, 705–715.
111. Sadler, K.E., Moehring, F., and Stucky, C.L. (2020). Keratinocytes contribute to normal cold and heat sensation. eLife *9*, e58625.
112. Gong, J., Liu, J., Ronan, E.A., He, F., Cai, W., Fatima, M., Zhang, W., Lee, H., Li, Z., Kim, G.H., et al. (2019). A Cold-Sensing Receptor Encoded by a Glutamate Receptor Gene. Cell *178*, 1375–1386.e11.
113. Cho, H., Yang, Y.D., Lee, J., Lee, B., Kim, T., Jang, Y., Back, S.K., Na, H.S., Harfe, B.D., Wang, F., et al. (2012). The calcium-activated chloride channel anoctamin 1 acts as a heat sensor in nociceptive neurons. Nat. Neurosci. *15*, 1015–1021.
114. Pinho-Ribeiro, F.A., Verri, W.A., Jr., and Chiu, I.M. (2017). Nociceptor Sensory Neuron-Immune Interactions in Pain and Inflammation. Trends Immunol. *38*, 5–19.
115. Abdus-Saboor, I., Fried, N.T., Lay, M., Burdge, J., Swanson, K., Fischer, R., Jones, J., Dong, P., Cai, W., Guo, X., et al. (2019). Development of a

Mouse Pain Scale Using Sub-second Behavioral Mapping and Statistical Modeling. Cell Rep. *28*, 1623–1634.e4.

116. Van Hees, J., and Gybels, J. (1981). C nociceptor activity in human nerve during painful and non painful skin stimulation. J. Neurol. Neurosurg. Psychiatry *44*, 600–607.
117. Klein, A., Solinski, H.J., Malewicz, N.M., Ieong, H.F., Sypek, E.I., Shimada, S.G., Hartke, T.V., Wooten, M., Wu, G., Dong, X., et al. (2021). Pruriception and neuronal coding in nociceptor subtypes in human and nonhuman primates. eLife *10*, e64506.
118. Liu, Q., Tang, Z., Surdenikova, L., Kim, S., Patel, K.N., Kim, A., Ru, F., Guan, Y., Weng, H.J., Geng, Y., et al. (2009). Sensory neuron-specific GPCR Mrgprs are itch receptors mediating chloroquine-induced pruritus. Cell *139*, 1353–1365.
119. Wang, F., Trier, A.M., Li, F., Kim, S., Chen, Z., Chai, J.N., Mack, M.R., Morrison, S.A., Hamilton, J.D., Baek, J., et al. (2021). A basophil-neuronal axis promotes itch. Cell *184*, 422–440.e17.
120. Yu, H., Zhao, T., Liu, S., Wu, Q., Johnson, O., Wu, Z., Zhuang, Z., Shi, Y., Peng, L., He, R., et al. (2019). MRGPRX4 is a bile acid receptor for human cholestatic itch. eLife *8*, e64506.
121. Meixiong, J., Vasavda, C., Snyder, S.H., and Dong, X. (2019). MRGPRX4 is a G protein-coupled receptor activated by bile acids that may contribute to cholestatic pruritus. Proc. Natl. Acad. Sci. USA *116*, 10525–10530.
122. Meixiong, J., Vasavda, C., Green, D., Zheng, Q., Qi, L., Kwatra, S.G., Hamilton, J.P., Snyder, S.H., and Dong, X. (2019). Identification of a bilirubin receptor that may mediate a component of cholestatic itch. eLife *8*, e44116.
123. Ma, Q. (2012). Population coding of somatic sensations. Neurosci. Bull. *28*, 91–99.
124. Sun, S., Xu, Q., Guo, C., Guan, Y., Liu, Q., and Dong, X. (2017). Leaky Gate Model: Intensity-Dependent Coding of Pain and Itch in the Spinal Cord. Neuron *93*, 840–853.e5.
125. Zheng, Q., Xie, W., Lückemeyer, D.D., Lay, M., Wang, X.W., Dong, X., Limjunyawong, N., Ye, Y., Zhou, F.Q., Strong, J.A., et al. (2022). Synchronized cluster firing, a distinct form of sensory neuron activation, drives spontaneous pain. Neuron *110*, 209–220.e6.
126. MacDonald, D.I., Luiz, A.P., Iseppon, F., Millet, Q., Emery, E.C., and Wood, J.N. (2021). Silent cold-sensing neurons contribute to cold allodynia in neuropathic pain. Brain *144*, 1711–1726.
127. Morita, T., McClain, S.P., Batia, L.M., Pellegrino, M., Wilson, S.R., Kienzler, M.A., Lyman, K., Olsen, A.S., Wong, J.F., Stucky, C.L., et al. (2015). HTR7 Mediates Serotonergic Acute and Chronic Itch. Neuron *87*, 124–138.
128. Delwig, A., Larsen, D.D., Yasumura, D., Yang, C.F., Shah, N.M., and Copenhagen, D.R. (2016). Retinofugal Projections from Melanopsin-Expressing Retinal Ganglion Cells Revealed by Intraocular Injections of Cre-Dependent Virus. PLoS One *11*, e0149501.
129. Choi, S., Hachisuka, J., Brett, M.A., Magee, A.R., Omori, Y., Iqbal, N.U., Zhang, D., DeLisle, M.M., Wolfson, R.L., Bai, L., et al. (2020). Parallel ascending spinal pathways for affective touch and pain. Nature *587*, 258–263.
130. Hasegawa, H., Abbott, S., Han, B.X., Qi, Y., and Wang, F. (2007). Analyzing somatosensory axon projections with the sensory neuron-specific Advillin gene. J. Neurosci. *27*, 14404–14414.
131. Badea, T.C., Cahill, H., Ecker, J., Hattar, S., and Nathans, J. (2009). Distinct roles of transcription factors brn3a and brn3b in controlling the development, morphology, and function of retinal ganglion cells. Neuron *61*, 852–864.
132. Lehnert, B.P., Santiago, C., Huey, E.L., Emanuel, A.J., Renauld, S., Africawala, N., Alkislar, I., Zheng, Y., Bai, L., Koutsioumpa, C., et al. (2021). Mechanoreceptor synapses in the brainstem shape the central representation of touch. Cell *184*, 5608–5621.e18.
133. Mali, P., Yang, L., Esvelt, K.M., Aach, J., Guell, M., DiCarlo, J.E., Norville, J.E., and Church, G.M. (2013). RNA-guided human genome engineering via Cas9. Science *339*, 823–826.
134. Hylden, J.L., and Wilcox, G.L. (1980). Intrathecal morphine in mice: a new technique. Eur. J. Pharmacol. *67*, 313–316.
135. Arshadi, C., Günther, U., Eddison, M., Harrington, K.I.S., and Ferreira, T.A. (2021). SNT: a unifying toolbox for quantification of neuronal anatomy. Nat. Methods *18*, 374–377.
136. Hein, L., Altman, J.D., and Kobilka, B.K. (1999). Two functionally distinct alpha2-adrenergic receptors regulate sympathetic neurotransmission. Nature *402*, 181–184.
137. Dubbs, A., Guevara, J., and Yuste, R. (2016). moco: Fast Motion Correction for Calcium Imaging. Front. Neuroinform. *10*, 6.

STAR★METHODS

KEY RESOURCES TABLE

REAGENT or RESOURCE	SOURCE	IDENTIFIER
Antibodies		
Chicken anti-GFP (1:500, IHC)	Aves Labs	GFP-1020; RRID:AB_10000240
Goat anti-GFP (1:500, IHC)	US Biological	G8965-01E
Goat anti-mCherry (1:500, IHC)	CedarLane	AB0040-200
Rabbit anti-CGRP (1:500, IHC)	Immunostar	24112; RRID:AB_2737130
Chicken anti-NEFH (1:500, IHC)	Aves Labs	NEFH
Rabbit anti-NEFH (1:500, IHC)	Sigma	N4142-.2ML; RRID:AB_477272
IB4 (Alexa 647 conjugated)	Invitrogen	I32450
Donkey anti-rabbit (Alexa fluor 488)	Invitrogen	A-21206; RRID:AB_2535792
Donkey anti-goat (Alexa Fluor 488)	Invitrogen	A-11055; RRID:AB_2534102
Donkey anti-rabbit (Alexa Fluor 546)	Invitrogen	A10040; RRID:AB_2534016
Donkey anti-chicken (Alexa Fluor 647)	Jackson	703-605-155; RRID:AB_2340379
Donkey anti-goat (Alexa Fluor 546)	Invitrogen	A11056; RRID:AB_2534103
Bacterial and virus strains		
AAV-FLEX-PLAP plasmid	Delwig et al.[128]	Addgene: 80422
AAV9-FLEX-PLAP viral prep	Janelia Viral Tools	N/A
AAV9-FLEX-GFP	This study	N/A
Chemicals, peptides, and recombinant proteins		
Tamoxifen	Sigma	T5648-1g
Sunflower seed oil	Sigma	S5007
Isofluorane	Henry Schein	029405
Paraformaldehyde (PFA), reagent grade, crystalline	Sigma	P6148-500G
Picric acid-formaldehyde (PAF) fixative (Zamboni)	Fisher	NC9335034
Normal Donkey Serum	Jackson	017-000-121
Deposited Data		
Single cell RNA sequencing dataset of dorsal root ganglia from mice of age P21-P24.	This study	GEO: GSE254789
Single cell RNA sequencing dataset of dorsal root ganglia from mice across developmental stages	Sharma et al.[28]	GEO: GSE139088
Experimental Models: Organisms/Strains		
Mouse: *Smr2*$^{T2a\text{-}Cre}$	This study	N/A
Mouse: *Sstr2*$^{CreER\text{-}T2a}$	This study	N/A
Mouse: *Adra2a*$^{T2a\text{-}CreER}$	This study	N/A
Mouse: *Cysltr2*^{Cre}	This study	N/A
Mouse: *Trpm8*$^{T2a\text{-}FlpO}$	This study	N/A
Mouse: *Oprk1*$^{T2a\text{-}Cre}$	This study	N/A
Mouse: *Bmpr1b*$^{T2a\text{-}Cre}$	Sharma et al.[28]	N/A
Mouse: *Ret*^{CreER}	Luo et al.[17]	N/A
Mouse: *TrkB*^{CreER}	Rutlin et al.[19]	MGI:5616440
Mouse: *TrkC*^{CreER}	Bai et al.[15]	MGI:97385
Mouse: *Th*$^{2A\text{-}CreER}$	Abraira et al.[27]	RRID:IMSR_JAX:025614
Mouse: *Mrgprd*^{CreER}	Olson et al.[30]	RRID:IMSR_JAX:031286
Mouse: *Mrgprb4*^{Cre}	Vrontou et al.[29]	RRID:IMSR_JAX:021077
Mouse: *Mrgpra3*^{Cre}	Han et al.[25]	N/A

(*Continued on next page*)

Continued

REAGENT or RESOURCE	SOURCE	IDENTIFIER
Mouse: *Calca-FlpE*	Choi et al.[129]	N/A
Mouse: *Advillin*^{FlpO}	Choi et al.[129]	N/A
Mouse: *Advillin*^{Cre}	Hasegawa et al.[130]	RRID:IMSR_JAX:032536
Mouse: *Sst*$^{IRES-Cre}$	Taniguchi et al.[62]	RRID:IMSR_JAX:013044
Mouse: Ai148 (TIT2L-GC6f-ICL-tTA2)	Jax	RRID:IMSR_JAX:030328
Mouse: Ai195 (TIT2L-GCaMP7s-ICF-IRES-tTA2)	Jax	RRID:IMSR_JAX:034112
Mouse: Ai95 (RCL-GCaMP6f)	Jax	RRID:IMSR_JAX:028865
Mouse: Ai96 (RCL-GCaMP6f)	Jax	RRID:IMSR_JAX:024106
Mouse: Ai65 (RCFL-tdT)	Jax	RRID:IMSR_JAX:021875
Mouse: *Brn3a*^{cKOAP}	Badea et al.[131]	RRID:IMSR_JAX:010558
Mouse: *Tau*^{FSFiAP}	Lehnert et al.[132]	N/A
Mouse: *R26*$^{LSL-ReaChR}$	Jax	RRID:IMSR_JAX:026294
Mouse: *R26*$^{FSF-LSL-ReaChR}$	Jax	RRID:IMSR_JAX:024846
Mouse: *R26*$^{LSL-Sun1/sfGFP}$ (INTACT)	Jax	RRID:IMSR_JAX:021039
Oligonucleotides		
Mm-Bmpr1b-C2	ACD bio	533941-C2
Mm-GCaMP6s-O1	ACD bio	557091
Mm-Sstr2-C2	ACD bio	437681-C2
Mm-Calca-tv2tv3-C2	ACD bio	420361-C2
Mm-Trpm8-C2	ACD bio	420451-C2
Mm-Cysltr2-C2	ACD bio	452621-C2
Mm-Sst	ACD bio	404631
ChR2-EYFP	ACD bio	519401
Primes and other RNAscope probes, see Table S1	N/A	N/A
Software and algorithms		
MATLAB	Mathworks	https://www.mathworks.com/products/MATLAB.html; RRID: SCR_001622
ImageJ	NIH	https://ImageJ.nih.gov/ij/

RESOURCE AVAILABILITY

Lead contact

Further information and requests for resources and reagents should be directed to and will be fulfilled by the lead contact, David Ginty (david_ginty@hms.harvard.edu).

Materials availability

Requests for mouse lines generated in this study should be directed to and will be fulfilled by David Ginty (david_ginty@hms.harvard.edu).

Data and code availability

- The DRG single-cell RNA sequencing dataset generated in this study has been deposited to the Gene Expression Omnibus (GEO: GSE254789). Other data reported in this study will be shared by the lead contact upon request.
- This paper does not report original code.
- Any additional information required to reanalyze the data reported in this paper is available from the lead contact upon request.

EXPERIMENTAL MODELS AND STUDY PARTICIPANT DETAILS

All experiments performed in this study were approved by the Institutional Animal Care and Use Committee (IACUC) of Harvard Medical School and Columbia University. Experiments followed the ethical guidelines outlined in the NIH Guide for the care and use of laboratory animals (https://grants.nih.gov/grants/olaw/guide-for-the-care-and-use-of-laboratory-animals.pdf). Male and female

mice of mixed genetic backgrounds were used for these studies. The ages of the animals for different experiments are indicated in the "method details" section. Mice were housed in a temperature-controlled and humidity-controlled facility, maintained on a 12h light/dark cycle, and given food and water ad libitum.

Mouse lines

Five of the mouse lines (*Smr2*$^{T2a\text{-}Cre}$, *Sstr2*$^{CreER\text{-}T2a}$, *Adra2a*$^{T2a\text{-}CreER}$, *Trpm8*$^{T2a\text{-}FlpO}$, *Oprk1*$^{T2a\text{-}Cre}$) were generated at the Gene Targeting and Transgenics Facility at Janelia Research Campus using standard homologous recombination techniques in hybrid mouse embryonic stem (ES) cells. These mouse lines were generated by knocking the T2a-(recombinase) cassette directly upstream of the stop codon in the last annotated exon of each indicated gene. *Sstr2* targeting was the exception as there were multiple annotated splice variants, therefore in this case, a (recombinase)-T2a cassette was knocked in directly downstream of the coding exon containing the methionine start codon for Sstr2. This design strategy was chosen to minimize potential deleterious consequences associated with deleting the gene. Chimeras were generated by blastocyst injection and germline transmission was confirmed by standard tail genotyping PCR. The neo selection cassette was left intact and each line was overtly phenotypically normal, even when bred as homozygous carriers of the knock-in allele, consistent with the introduction of the T2a-recombinase cassette minimally perturbing endogenous gene expression.

To generate *Cysltr2*$^{T2a\text{-}Cre}$, a guide RNA (GAATTTCAAAGCTCGATTAA) was designed specific for the 3′ region of the murine Cysltr2 locus close to the STOP codon. sgRNA was generated by *in vitro* transcription using the MEGAshortscript T7 Transcription Kit from Invitrogen (cat. # AM1354) from a template carrying a T7 promoter, guide RNA and an RNA scaffold (based on Mali et al.[133]) encoding the sgRNA. The Cas9 mRNA was generated using the mMACHINE T7 Transcription Kit from Invitrogen (cat. # AM1344) from a template carrying a T7 promoter and a sequence encoding Cas9. Both, the sgRNA and Cas9 mRNA were purified using the MEGAclear Transcription Clean-Up Kit (cat. # AM1908). An embryo injection mix was prepared with the following components: (1) DNA donor molecule carrying a Cysltr2-2A-Cre recombinase targeting construct (100ng/ul) (2) sgRNA (112ng/ul) (3) Cas9 mRNA (100ng/ul). The DNA donor molecule was sequenced beforehand to confirm sequence fidelity. Embryos on the C57Bl/6 genetic background were injected. A chimeric founder mouse was identified by PCR interrogating the left and right integration sites of the targeting construct with the following primer combinations: MP319 and MP320 (left junction) yielding an 846bp product and MP302-MP317 (right junction) yielding a 554bp product. PCR products were TOPO cloned and sequenced to confirm faithful integration of the targeting construct. To investigate the possibility of unwanted, off-target activity of the injected CRISPR/Cas9 mix, we performed off-target analysis on the top 10 predicted off-targets and one additional off-target located within a gene (off-target 20). Specifically, we designed PCR primers around these predicted sites and sequenced the PCR products. Our analysis indicated that no edit occurred in this set of highest probability off-targets.

Genotyping

For the mouse lines generated in this paper, the following allele-specific primers are used:

Smr2$^{T2a\text{-}Cre}$:
Genome forward: ACTGCTACTGCCCCCAATTCTACTG
Cre reverse: ATCGCGAACATCTTCAGGTTCTGC
Genome reverse: GTAGCTGATATTGAAGGTGTCATGGTAC
Expected band size for mutant: 302bp
Expected band size for wild-type: 583bp

Sstr2$^{CreER\text{-}T2a}$:
Genome forward: TCCGTCAATAAAGCACCTGACTTGC
CreER forward: TGGAGGAGACGGACCAAAGCCACT
Genome reverse: AGCCGTTGAGGTCAAATGGAGAGG
Expected band size for mutant: 231bp
Expected band size for wild-type: 346bp

Adra2a$^{T2a\text{-}CreER}$:
Genome forward: GCTCGCTGAACCCTGTTATCTACAC
CreER reverse: CGAACCTCATCACTCGTTGCATCG
Genome reverse: CTCATGTGTCCCTCTCAGCCAGAAC
Expected band size for mutant: 221bp
Expected band size for wild-type: 284bp

Trpm8$^{T2a\text{-}FlpO}$:
Genome forward: CTTCCAAGCTTAACGACCTCAAAAGTC
Flpo reverse: CACAGGATGTCGAACTGGCTCATC
Genome reverse: CTGCTTCTTGTCTCTAGACCATGAC
Expected band size for mutant: 160bp
Expected band size for wild-type: 269bp

Oprk1$^{T2a\text{-}Cre}$:

Genome forward: CCTATTAAGATGCGAATGGAGCGCC
Cre reverse: TGCAGGCAAATTTTGGTGTACGGTC
Genome reverse: CTCAAGGGATTGAAATCGGCTTGGC
Expected band size for mutant: 411bp
Expected band size for wild-type: 195bp
Cysltr2$^{T2a\text{-}Cre}$:
MP302 (right junction): TGGTTTGTCCAAACTCATCAA
MP317 (right junction): AAATCAAAGCCTGCTCCAGA
The primer pair of MP302 and MP317 should give product of 554bp for *Cysltr2*$^{T2a\text{-}Cre}$ allele.
MP318 (left junction): GTCACCAGTGTCAGGAGTGC
MP320 (left junction): TCCCTGAACATGTCCATCAG
The MP318 and MP320 primer pair should yield a 710bp product for the *Cysltr2*$^{T2a\text{-}Cre}$ allele.

Tamoxifen treatment

Tamoxifen was dissolved as previously described.[15] The dose and timing of tamoxifen treatment for non-sparse labeling are: for *Sstr2*$^{CreER\text{-}T2a}$ and *MrgprD*^{CreER}, 3mg of tamoxifen was delivered at 2-3 weeks old (i.p.); for *Th*$^{2A\text{-}CreER}$, 3mg of tamoxifen was delivered at 3 weeks old (i.p.); for *Adra2a*$^{T2a\text{-}CreER}$, 4mg of tamoxifen was delivered at 2 weeks old (i.p); for *TrkB*^{CreER}, 0.5mg of tamoxifen was delivered at postnatal day 4-5 (i.p.); for *Ret*^{CreER}, 3mg of tamoxifen was delivered via oral gavage to pregnant females at embryonic day E10.5-E12.5; for labeling of Aβ SA1-LTMRs by *TrkC*^{CreER}, 3mg of tamoxifen was delivered via oral gavage to pregnant females at embryonic day E12.5; for labeling of Aβ Field-LTMRs by *TrkC*^{CreER}, 0.1mg of tamoxifen was delivered at postnatal day 5 (i.p.). The dose of tamoxifen for sparse labeling is indicated in the STAR Methods section of "sparse labeling for single-neuron morphological analysis".

METHOD DETAILS

Single-cell RNA-seq

The dissection strategy used was essentially as previously described.[28] Briefly, animals were sacrificed at approximately postnatal day 21 and spinal columns rapidly removed and placed on ice. Individual DRG with central and peripheral nerves attached were removed from all axial levels and placed into ice-cold DMEM:F12 (1:1) supplemented with 1% pen/strep and 12.5 mM D-glucose. A fine dissection was performed to remove the peripheral and central nerve roots, resulting in only the sensory ganglia remaining. scRNA-seq experiments are the culmination of six independent bioreplicates. Sensory ganglia were dissociated in 40 units papain, 4 mg/ml collagenase, 10 mg/ml BSA, 1 mg/ml hyaluronidase, 0.6 mg/ml DNase in DMEM:F12 + 1% pen/strep + 12.5 mM glucose for 25 min at 37 °C. Digestion was quenched using 20 mg/ml ovomucoid (trypsin inhibitor), 20 mg/ml BSA in DMEM:F12 + 1% pen/strep + 12.5 mM glucose. Ganglia were gently triturated with fire-polished glass pipettes (opening diameter of approx. 150–200 μm). Neurons were then passed through a 70-μm filter to remove cell doublets and debris. Neurons were pelleted and washed 4 times in 20 mg/ml ovomucoid (trypsin inhibitor), 20 mg/ml BSA in DMEM:F12 + 1% pen/strep + 12.5 mM glucose followed by 2× washes with DMEM:F12 + 1% pen/strep + 12.5 mM glucose all at 4 °C. After washing, cells were resuspended in 45 μl of DMEM:F12 + 1% pen/strep + 12.5 mM glucose.

scRNA-seq analysis

Alignment, mapping, and general quality control was performed using the 10x genomics cell ranger pipeline. This pipeline generated the gene expression tables for individual cells used in this study. Briefly, ~8000-10000 dissociated cells from DRG were loaded per 10x run (10x genomics chromium single cell kit, v3). Downstream reverse transcription, cDNA synthesis and library preparation were performed according to manufacturer's instructions. All samples were sequenced on a NextSeq 550 with 58bp sequenced into the 3' end of the mRNAs. As quality control filter, individual cells were removed from the dataset if they had fewer than 1,000 discovered genes, fewer than 1,000 unique molecule identifiers (UMIs) or more than 10% of reads mapping to mitochondrial genes. Non-neuronal cells were also removed from our analysis. Neuronal subtypes were identified as clusters using PCA/UMAP analysis combined with prior studies identifying marker genes for distinct DRG neuron subtypes. Non-neuronal cells were identified in one of two ways. In the first, if the cells contained prominent markers of endothelial or Schwann cells (Sox2, Ednrb) they were removed. In the second, if a cluster was clearly devoid of DRG sensory neuron markers (Pou4f1, Avil), they were also removed. Generally, we found approximately 20-25% of cells recovered showed signatures of non-neuronal identity based on these criteria. Differential gene expression analysis was performed on all expressed genes using the FindMarker function in Seurat using the Wilcoxon rank-sum test and a pseudocount of 0.001 was added to each gene to prevent infinite values. P values $<10-322$ were defined as 0, as the R environment does not handle numbers $<10-322$. Individual cell gene expression values were removed in the violin plots to allow for clarity due to the large number of cells.

AAV production and neonatal IP injection

AAV genome plasmids were constructed using standard cloning and molecular biology techniques. AAV (serotype 2/9) were packages and concentrated using transient transfection of pRC9, pHelper and AAV-genome plasmid into 6-12 T225 flasks of HEK 293T cells. Viral containing supernatants were collected at 72 and 120 hours post-transfection. 120 hours post-transfection, cells were

scraped off plates and collected. AAV producing 293T cell pellets were extracted using a lysis buffer containing salt active nuclease (articzymes) in 40 mM Tris, 500 mM NaCl and 2 mM $MgCl_2$ pH 8 (referred to as SAN buffer). Viral supernatants were concentrated via 8% PEG/500 mM NaCl precipitation and ultimately re-suspended in SAN buffer. Cleared viral lysates were then loaded onto a density gradient (optiprep) and subsequently concentrated using Amicon filters with a 100-kD molecular cutoff to a final volume of approximately 25-30uL. AAVs (2/9) were injected intraperitoneally (IP) into pups at P1-2. Pups were transiently anaesthetized by hypothermia and beveled pipettes were used to deliver between 10^{11} and 10^{12} viral genomes in a volume of 10 μl (1 × PBS supplemented with 0.01% Fast Green, 35mM NaCl, 5% Glycerol). Skin, DRG, or spinal cord samples were collected from animals at least 3 weeks after AAV mediated transduction.

Immunohistochemistry

We used a similar protocol as previously described.[28] Animals were perfused with PBS then 4% PFA. Spinal column was dissected out and fixed in 4% PFA overnight (4°C). Hairy skin on the thigh or back was dissected out, treated with Nair Hair Removal Lotion, and rubbed with tissue paper until all hair was removed. The skin was then washed and fixed in Picric acid-formaldehyde (PAF) fixative (Zamboni) overnight (4°C). After tissue fixation, the tissue was embedded in OCT (14-373-65, Fisher), frozen and stored in -80°C freezer. Upon cryosection, the tissue was sectioned with the thickness of 25 or 30 micron and mounted on Superfrost plus slides (12-550-15, Fisher). After drying in room temperature (RT) overnight, the slides were rehydrated and washed by PBS, and blocked by 5% Normal Donkey Serum for 2 hours at RT. Then primary antibody mix was added for 2 hours at RT or 1-2 days at 4°C. After washing the primary antibody with 0.02% PBS-Triton, the secondary antibody mixed was added for 2 hours at RT or 1-2 days at 4°C. At last, the slides were washed in PBS, mounted using DAPI Fluoromount-G (0100-20, Southern Biotech), and imaged using a confocal microscope (Zeiss LSM 700 or Zeiss LSM 900).

When measuring DRG neuron diameter, individual DRG neuron cell bodies with DAPI signal were manually outlined in ImageJ, and the diameter was calucted from area of the cell bodies. For each DRG neuron subtypes, multiple DRGs from multiple animals were quantified.

Quantification of spinal cord terminals

The transverse sections of lumbar spinal cord were stained for CGRP, IB4 and reporter proteins (tdTomato or GFP). After the fluorescence images were taken under a confocal microscope, multiple lines were drawn in ImageJ, perpendicular to the surface of spinal cord, from the surface of lamina I to the deeper laminae. The corresponding images and locations of the lines were then loaded into MATLAB, the intensity of the fluorescence signal from different channels (CGRP, IB4 and reporter) were measured across 100 lines, which were linearly created between the lines in ImageJ, to ensure dense sampling and provide a better representation of the fluorescence intensity across different laminae. To account for minor size differences between sections, we aligned the peak of CGRP and IB4 of different images, and adjusted the depth of the reporter signal accordingly. The reporter signals from multiple sections of the same DRG neuron subtype were then averaged. The heatmap showing the intensity of CGRP, IB4 and reporter signals was plotted using MATLAB.

In situ hybridization (RNAscope)

We used a similar protocol as previously described[28] following the recommended protocol from ACD bio website (https://acdbio.com/manual-assays-rnascope). DRGs were freshly dissected out of the animals, embedded in OCT and flash frozen. After cryosection at 25-micron thickness, the slides were fixed in 4% prechilled PFA in 4°C for 15 mins, then dehydrated using serial concentrations of ethanol. Next the sections were digested using Protease IV for 30 mins at RT. After washing, mix of RNAscope probes was added on the slide and incubated at 40°C for 2 hours, followed by adding and washing Amp1, Amp2, Amp3 and Amp4 sequentially according to the protocol. At last, the slides were mounted using DAPI Fluoromount-G (0100-20, Southern Biotech), and imaged using a confocal microscope (Zeiss LSM 700 or Zeiss LSM 900). Quantifications of the images were performed in ImageJ. Cells with clear fluorescent puncta were defined as positive for the corresponding RNA.

Sparse labeling for single-neuron morphological analysis

For sparse labeling experiments, the available CreER lines were crossed to $Brn3a^{cKOAP}$ mice, and the sparsity was controlled by tamoxifen dose. Aβ field-LTMRs or Aβ SA1-LTMRs were labeled using $TrkC^{CreER}$ treated with 0.01mg tamoxifen at P8. Aβ RA-LTMRs were labeled using Ret^{CreER} treated with 0.03mg tamoxifen at E11.5. Aδ-LTMRs were labeled using $TrkB^{CreER}$ treated with 0.005mg tamoxifen at P5. C-LTMR were labeled using $TH^{2A\text{-}CreER}$ with 0.2mg tamoxifen at P21. $Sstr2^{CreER\text{-}T2a}$; $Brn3a^{cKOAP}$ mice were given 0.1mg tamoxifen at P14. Sparse labeling of MRGPRD$^+$ neurons relied on the leaky expression of $MrgprD^{CreER}$ without using tamoxifen.

For the sparse labeling in Cre lines, AAV9-FLEX-FLAP was injected into back hairy skin using reported procedure[132] or intrathecally as previously described.[134] Back hairy skin injections were done in P9-P14 animals with a total volume of 2ul AAV injected into 4-6 spots across the back. Undiluted AAV (titer $1.2*10^{13}$ gc/mL) was used for $Cylstr2^{Cre}$ mice, while a 4X dilution was used for $Bmpr1b^{Cre}$ and $Smr2^{Cre}$ mice. Intrathecal (i.t.) injections were done in $Mrgprb4^{Cre}$ or $Mrgpra3^{Cre}$ mice that were 3-4 weeks old using 5 ul undiluted AAV9-CAG-FLEX-PLAP virus. For sparse labeling using $Trpm8^{FlpO}$ mice, 2ul of AAV9-fDIO-FLAP was injected into back hairy skin of $Trpm8^{FlpO}$ animals that were 9-12 days old. The animals were perfused 1-3 weeks after injection of tamoxifen or AAV.

Whole-mount alkaline phosphatase staining of the skin and spinal cord

Whole-mount placental alkaline phosphatase staining protocol was adapted from a previous report.[132] Animals of 4-6 weeks old were perfused in PBS then 4% PFA, then NAIR is applied on hairy skin on the back and thigh of the animals. After overnight fixation in Zamboni fixative (phosphate buffered picric acid-formaldehyde) at 4°C, tissue was washed in PBS and incubated at 65-68°C for 2-2.5 hours to inactivate the endogenous alkaline phosphatase activity, then washed with B3 buffer (0.1M Tris pH 9.5, 0.1M NaCl, 50mM $MgCl_2$, 0.1% Tween-20) at room temperature. The substrate, NBT/BCIP (3.4μL per ml of B3 buffer), was added to start the reaction. After 8-24 hours (depending on the expression level) at room temperature, tissue was washed in B3 buffer and pinned down in dishes before fixation in 4% PFA for one hour in room temperature. After fixation, dehydration started with putting the tissue 50% ethanol (1 hour), then 75% ethanol (1hour), at last 100% ethanol for 3 times, with overnight dehydration in the last time of 100% ethanol. After complete dehydration, tissue was cleared in BABB (Benzyl Alcohol: Benzyl Benzoate = 1:2) at room temperature for 30 mins. The tissue was then imaged under a Zeiss AxioZoom stereoscope. After imaging, the tissue was stored in 100% ethanol at 4°C.

Quantification of skin arborizations in the sparse labeling experiments

The skin was flattened before imaging, and a Z-stack image was taken to cover the depth of the skin. Only arborizations that clearly belong to a single neuron were imaged. *Smr2*$^{T2a\text{-}Cre}$ labeled neurons could also show lanceolate endings and circumferential endings although uncommon, which were excluded in the quantification because we focus on the SMR2/CGRP^{+} population that only showed free-nerve endings using *Smr2*$^{T2a\text{-}Cre}$;*Calca-FlpE* intersection (Figure S5). The arborization area was measured in ImageJ by drawing a polygon tightly around the skin arbors. The axonal branch points were counted manually. Reconstruction of skin arborizations was done using SNT plugin.[135]

Axial level analysis of *Adra2a*$^{T2a\text{-}CreER}$ labeling

Tamoxifen was administrated (i.p.) to *Adra2a*^{CreER}; *Brn3a*^{cKOAP} animals at P14 and P16 age, using a total dose of 4mg. Using *Brn3a*^{cKOAP} reporter line avoids labeling of sympathetic fibers, which express Adra2a.[136] Animals were perfused 2-3 weeks later. Cutaneous skin, various internal organs and spinal column were dissected out and fixed overnight at 4°C in either 4% PFA or Zamboni fixative. Spinal cord was dissected out carefully with most DRGs attached. The Whole-mount placental alkaline phosphatase staining protocol was the same as described above. After clearing with BABB, the DRGs attached to the spinal cord were imaged under a Zeiss AxioZoom stereoscope with Z-stack covering the depth of all DRGs. The L4/L5 DRGs were defined as the two large ganglion that connected to the two thickest nerves in lumbar level. The axial level of the other DRGs were based the relative distance (in the number of segments) to L4/L5. The number of labeled DRG cells were manually counted in ImageJ, although the dense labeling of certain DRGs (especially from T10-L1 level) and the resolution of the stereoscope would cause underestimation of cell numbers or render the image indiscernible. The cell counts from left and right DRGs of the same level were averaged for the same animals. There were occasional loss of DRGs during tissue processing, leading to variation of the number of datapoints for each axial level.

In vivo epifluorescence calcium imaging

The mice of either sex at 3-6 weeks were anesthetized with inhalational isoflurane (1.8-2.3%) throughout the experiments. Body temperature was maintained at 37°C ± 0.5°C on a custom-made surgical platform. The back hair was shaved, and an incision was made over the lumbar vertebrae. Paravertebral muscles along L4 vertebral spine were dissected, then the bone on top of L4 DRG was removed by rongeur or by bone drill. Surgifoam sponges (Cat# 1972, Mckesson) and cotton was used to stop the bleeding. Custom-made spinal clamp was used to stabilize the spinal column.

The surgical preparation was then transferred to the platform under an upright epifluorescence microscope (Zeiss Axio Examiner) with 10X air objective (Zeiss Epiplan, NA=0.20). The light source is 470nm LED (M470L5, Thorlabs) with LED driver (LEDD1B, Thorlabs). A CMOS Camera (CS505MU1, Thorlabs) was triggered at 10 frames per second with a 50ms exposure time. All the recorded stimuli were synchronized with the camera and LED using a DAQ board (National Instrument, NI USB-6343).

Stimuli applications

For assessment of mechanical thresholds using step indentation, receptive fields of a certain neuron within field of view were explored using a blunt probe. If a point gave the most robust calcium signal increase, the indenter was then placed on top of the point. Indentation was delivered using a mechanical stimulator (300C-I, Aurora Scientific) with a custom-made indenter tip with an end of ~200um in diameter. The duration of indentation was 0.5 second for all experiments, except when examining the adaption properties, the indentation duration was increased to 3 seconds. The interval between indentation steps was set at least 6 seconds to allow the calcium signal to return baseline.

For assessment of polymodality, a square region (12.5*12.5 mm) on the mouse thigh was specified for all the following mechanical, electrical, and thermal stimuli. Air puff (1PSI) was first delivered to the region. Then the stroke stimuli were delivered by cotton swab mounted vertically on a miniature load cell for force measurement (Model MBL, 50gram, Honeywell). The load cell was calibrated using standard weight. The force of stroke stimuli was maintained below 50mN. Next 6-gram, 10-gram and 26-gram Von Frey filaments (North Coast Medical) were applied on the same skin region sequentially. To fully cover the skin region for mechanical stimuli, a custom made Von Frey array was used. Individual 8-gram Von Frey filaments were made from Carbon Fiber (2004N11, McMaster

Carr) by adjusting the length of the filament and indenting on a digital scale. Twenty-five of such filaments were mounted on a piece of acrylic (13*13 mm) in even distribution. The other side of the acrylic was connected to a manipulator (U-3C, Narishige). The last mechanical stimulation is pinch, which was delivered by a pair of cover glass forceps (11074-02, FST). A pair of FlexiForce sensor (A101, Tekscan) were mounted on the flat inner tip of the forceps, with rubber pads (15mm^2) mounted on the sensor for better measurement. The force delivered by pinch were within 2-4 N range. Hair on the thigh was kept during air puff and stroke to preserve the natural condition and shaved before using Von Frey filament and pinch stimuli for better spatial accuracy. All the mechanical stimuli were applied after 10 seconds of baseline recording and lasted 20 seconds during which various spots across the selected skin region were stimulated intermittently.

Electrical stimuli were applied using custom-made bipolar electrode controlled by a Current Stimulator (DS3, Digitimer) triggered at 10 pulses per second. The stimulation intensity was no more than 1mA with a duration of 2ms for each pulse. The tip of bipolar electrode and skin was lighted dampened before the stimulation. The stimulation locations were changed within the selected skin region to cover the region, lasting no more than 30 seconds in total.

For thermal stimuli, a Peltier device (13*12*2.5mm, TE-65-0.6-0.8, TE technology) was controlled by a Temperature Controller (TEC1089/PT1000, Meerstetter Engineering) with an RTD Platinum (Pt) thermistor (2952-P1K0.161.6W.A.010-ND, Digikey) mounted on the surface of Peltier. A copper bar (12.7*12.7*60mm) was mounted on the other side of the Peltier device using double-sided thermal tape, acting as a heatsink. The heatsink was connected to a manipulator (U-3C, Narishige) for positioning of the Peltier device. Before thermal stimuli, ~50ul of thermal paste (Thermal Grizzly, Aeronaut) was evenly applied on the top of the Peltier surface, which was then gently pressed on the skin until good contact was formed, thus the thermal conductivity between the Peltier device and skin could be maximized. A thermocouple microprobe (IT-1E, Physitemp) was inserted between Peltier device and skin as a separate measurement of the applied temperature. Thirty seconds after contacting skin, temperature stimuli started from innocuous temperatures progressing to noxious temperatures, in the sequence of 35, 25, 20, 40, 15, 45, 10, 50, 5, 55°C. Each temperature step started with a baseline of 20 seconds holding at 32°C, then to the target temperature for 20 seconds, and back to the baseline (32°C) holding for 50 seconds before the next temperature step. The change rate for all temperatures was kept at 5°C s^{-1}.

Calcium Imaging analysis

For imaging analysis, motion correction and spatial high-pass filtering was conducted using a custom-written macro code that employed ImageJ plugin "moco[137]" and "Unsharp mask" filter, then regions of interest (ROIs) were manually picked. Cells with baseline signal and/or with calcium response were picked and aligned across videos from various stimuli. The generated intensity measurement from ImageJ was further analyzed using MATLAB. In the calculation of ΔF/F, F was defined using baseline activity (average intensity before each stimulation). The mechanical threshold for each indentation session was determined by the first distinguishable calcium spikes aligned with step indentation. The amplitude of indentation step was determined by the maximum calcium peak (ΔF/F) within 0.5 seconds after the end of indentation step. The response amplitudes for air puff, stroke, Von-Frey filament, and pinch were calculate as the maximum calcium response within the session. The warm/heat threshold was determined by the corresponding ascending temperature step where the first calcium spike occur, while the cooling/cold threshold was determined by the corresponding descending temperature step where the first calcium spike occur. The amplitude of thermal response was calculated as the maximum calcium peak aligned within each temperature step for the thermal sensitive cells.

For the polymodality plot (Figure 7), first we established three vectors for tuning to mechanical, heat and cold, respectively, each 120 degrees apart with a distinct color vector. Then the maximal responses to mechanical, heat and cold from the same neurons were extracted. To determine the color of each point in the scatter plot, the maximal response to each modality was normalized to the summation of the maximal responses of all three modalities of each neuron. The dot product of the color vector and the corresponding normalized response vector gave the color of each dot. To determine the location of each point, log scale was applied to the magnitude of maximal response, to compress the range for visualization. The dot product of the direction vector of each modality and the corresponding log scale magnitude decided the location of each neuron in the scatter plot.

QUANTIFICATION AND STATISTICAL ANALYSIS

Statistical analyses were conducted using GraphPad Prism (Version 9, GraphPad Software). The number of mice and the statistical tests used for individual experiments are included in the figure legends. One-Way ANOVA with Dunnett's Correction Post Hoc Test was used in Figures S4D and S4E.

CellPress
OPEN ACCESS

Supplemental figures

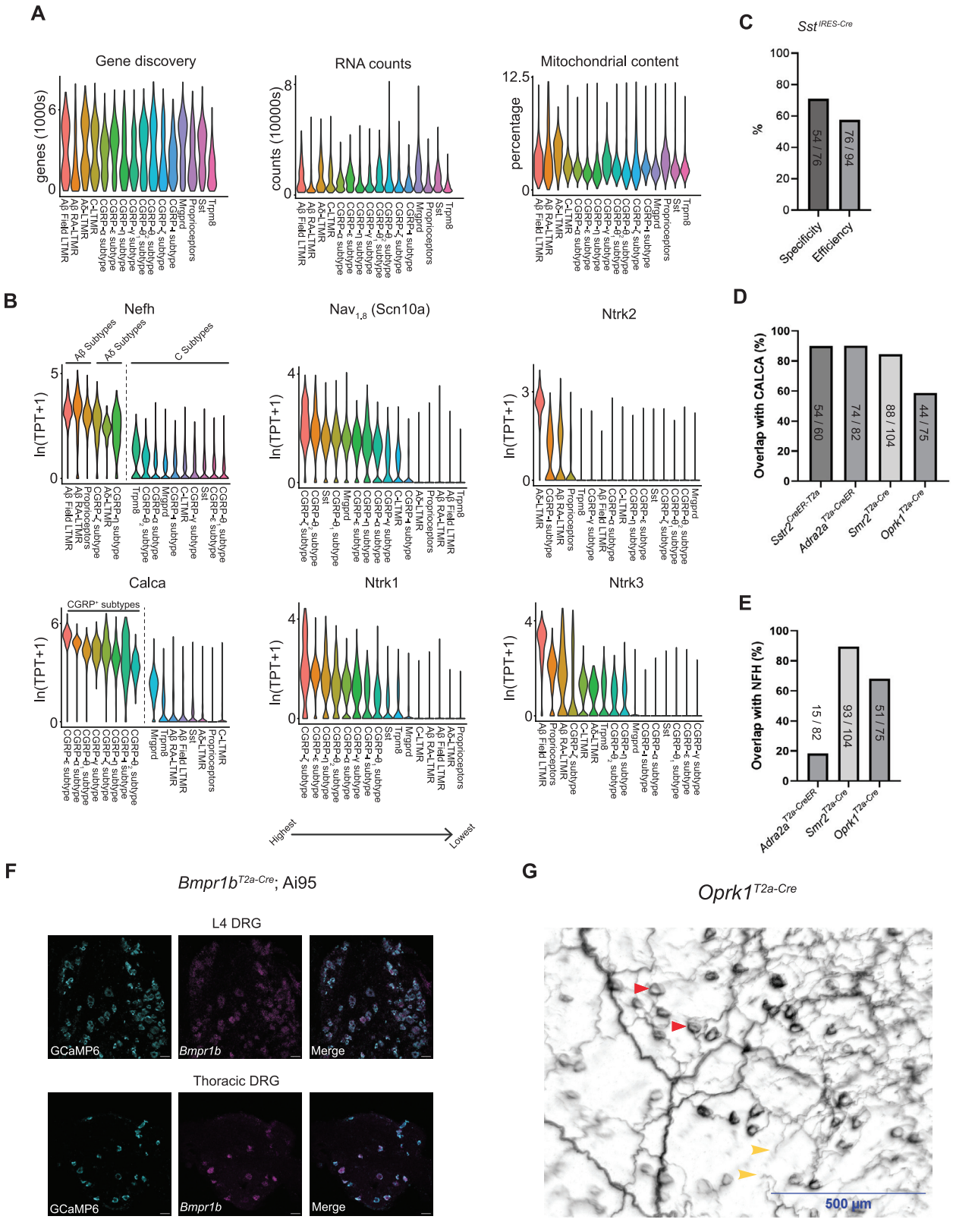

(legend on next page)

Figure S1. Additional characterization of the scRNA-seq dataset and genetic tools, related to Figure 1

(A) Additional QC metrics and descriptive statistics for the scRNA-seq data.

(B) The expression of common marker genes in transcriptionally defined DRG neuron subtypes.

(C) The specificity and efficiency of genetic labeling in *Sst*$^{IRES\text{-}Cre}$; *R26*$^{LSL\text{-}Sun1/sfGFP}$ mice, determined by RNAscope. Specificity and efficiency were defined as described in Figure 1D.

(D and E) The overlap with Calca (D) and NEFH (E) in DRG neurons labeled using genetic tools and examined by RNAscope.

(F) RNAscope of DRGs from *Bmpr1b*$^{T2a\text{-}Cre}$; Ai95 mice reveals higher number of neurons per section that are labeled in L4/L5 DRG compared with thoracic DRGs. Scale bars, 50 μm.

(G) AP staining of hairy skin from *Oprk1*$^{T2a\text{-}Cre}$ animals injected with Cre-dependent AP virus (intrathecal injection at 3 weeks old) shows labeling of multiple types of skin terminals, including circumferential endings (red arrows) and free-nerve endings (yellow arrows).

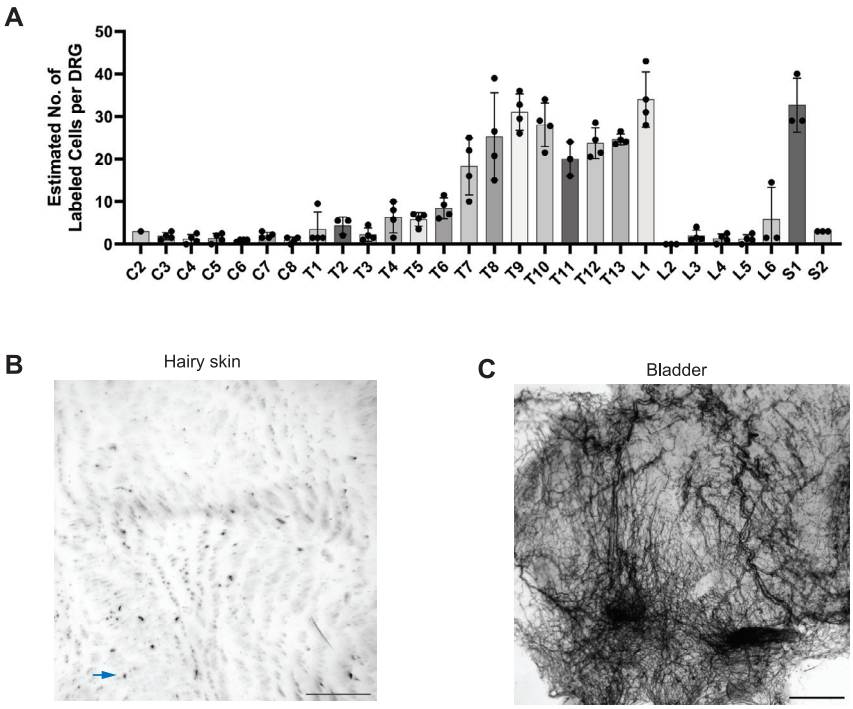

Figure S2. *Adra2a*$^{T2a\text{-}CreER}$-labeled neurons (CGRP-γ) innervate internal organs but not the skin, related to Figure 1

(A) Estimated number of labeled DRG neurons across different axial levels using *Adra2a*$^{T2a\text{-}CreER}$; *Brn3a*^{cKOAP} mice and whole-mount AP staining of spinal cords with DRGs attached. Each data point is the averaged number between left and right DRG of the same axial level from the same animal (4 animals in total). DRGs that were lost or that were too dense to count in the whole-mount staining were not included. Error bar, SD.

(B) Examples of whole-mount AP staining of back hairy skin. The arrow points to the typical background signal. Only a total of 1–5 cutaneous neurons were identified from each animal.

(C) Example of whole-mount AP staining of the bladder (C). Scale bars: 1 mm in (B) and (C).

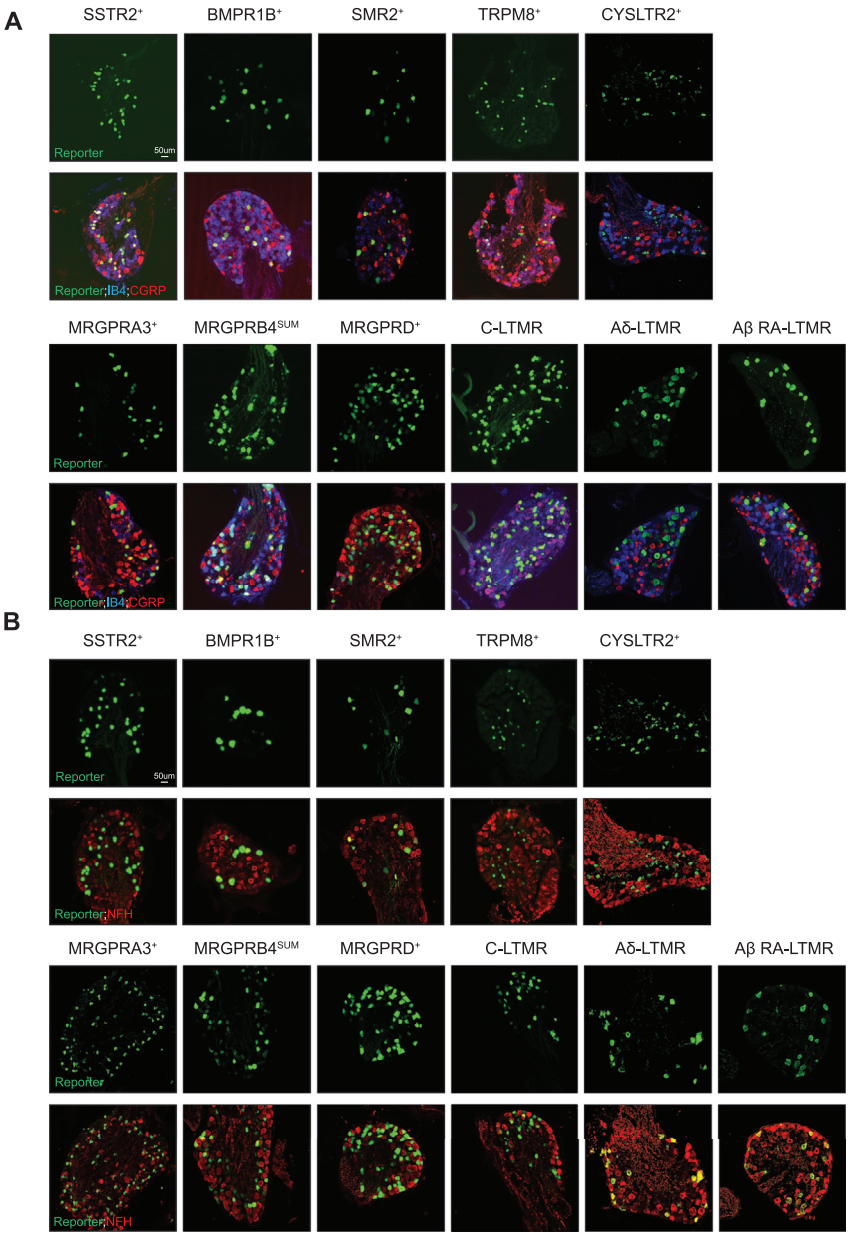

C

	NFH overlap	IB4 overlap	CGRP overlap
BMPR1B+	88.89%	0.00%	93.33%
CYSLTR2+	0.00%	5.56%	0.00%
MRGPRA3+	10.53%	15.79%	26.32%
MRGPRB4SUM	17.39%	30.43%	15.38%
MRGPRD+	0%	94.12%	3.85%
Aβ RA-LTMR	90.00%	6.25%	4.35%
SMR2+	88.89%	0.00%	88.89%
SSTR2+	7.14%	0.00%	90.48%
C-LTMR	6.67%	0.00%	4.76%
Aδ-LTMR	82.35%	5.88%	3.03%
TRPM8+	5.88%	0.00%	0.00%

D

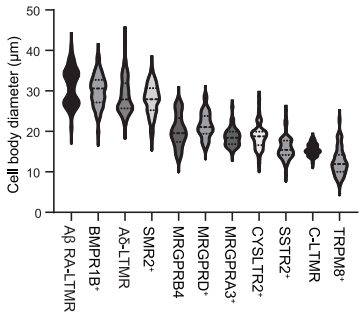

(legend on next page)

Figure S3. Immunohistochemical analysis of DRG sensory neuron subtypes, related to Figure 1

(A) DRG sections obtained from the mice harboring the recombinase alleles generated in this study (top row) and previously established alleles (bottom row) were co-stained with the reporter, CGRP, and IB4.

(B) DRG sections obtained from the recombinase alleles generated in this study (top row) and previously established alleles (bottom row) were co-stained with the reporter and NEFH.

(C) Quantification of the percent overlap of labeled cells with respect to CGRP (A), IB4 (A), and NEFH (B).

(D) Quantification of the cell body diameter across the DRG subtypes. n = 48, 54, 53, 57, 51 59, 55, 48, 65, 48, 50 (from left to right). All scale bars, 50 μm.

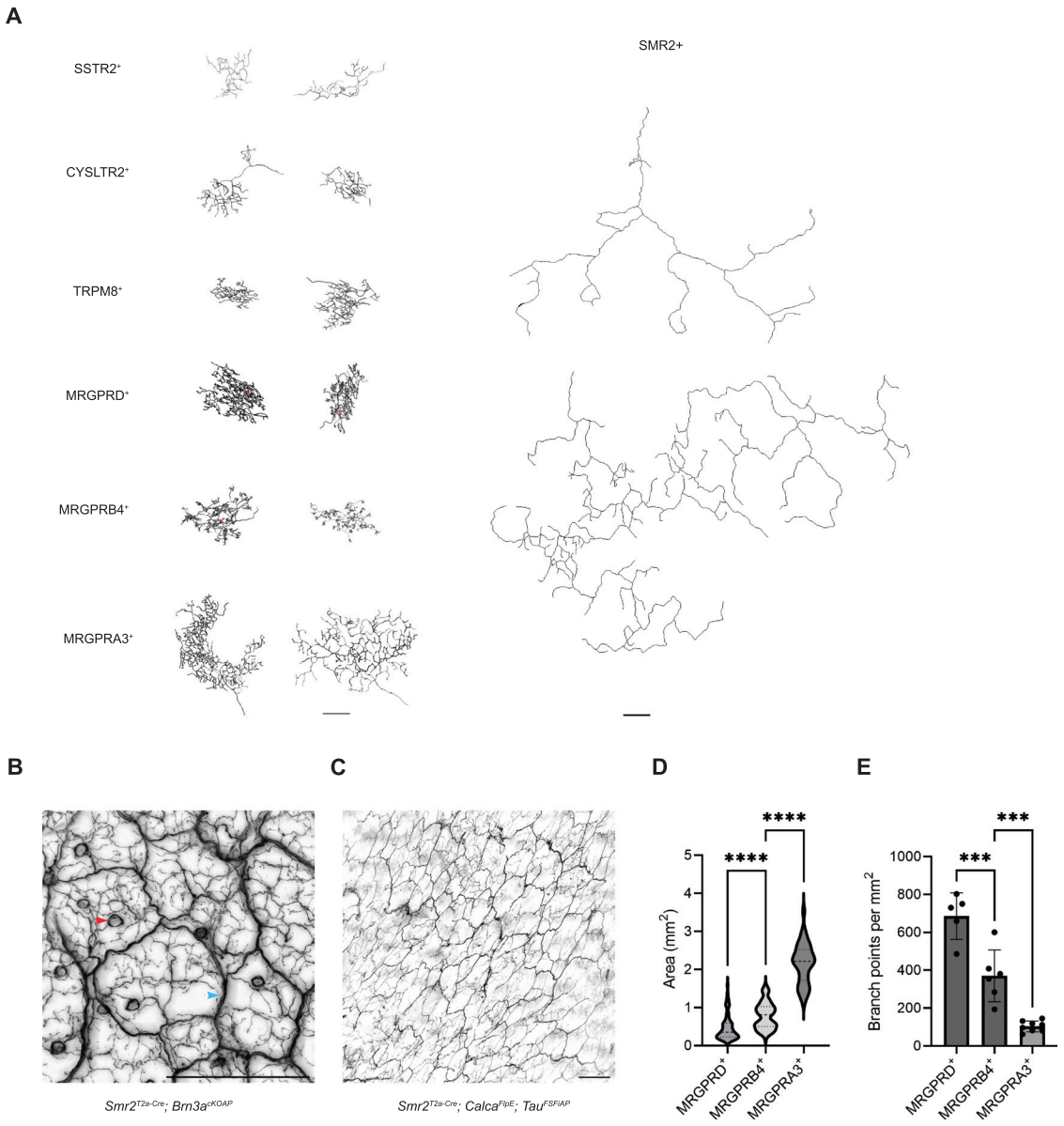

Figure S4. Morphological diversity of free-nerve endings, related to Figure 2

(A) Additional reconstructed examples of individual free-nerve ending neurons across the different populations. Arrows in magenta point to the "circumferential-like" terminals of MRGPRD$^+$ and MRGPRB4$^+$ neurons.

(B) *Smr2*$^{T2a\text{-}Cre}$; *Brn3a*^{cKOAP} occasionally labels circumferential endings (red arrow). Blue arrow points to the thick nerve fiber under the epidermis.

(C) Intersection genetic labeling strategy using *Smr2*$^{T2a\text{-}Cre}$; *Calca-FlpE*; *Tau*^{FSFiAP} mice is specific for labeling CGRP-ζ (SMR2$^+$) populations, only showing free-nerve endings.

(D and E) Comparison of the arborization area (D) and branching density (E) for MRGPRD$^+$ (n = 76), MRGPRB4$^+$ (n = 95), and MRGPRA3$^+$ (n = 40) neurons. One-way ANOVA with Dunnett's correction post hoc tests, ****$p < 0.0001$, ***$p < 0.001$. In (D), main effect $F(2, 208) = 274.5$. In (E), main effect $F(2, 16) = 52.75$. Error bars in (E) indicate the standard deviation.

All scale bars, 500 μm.

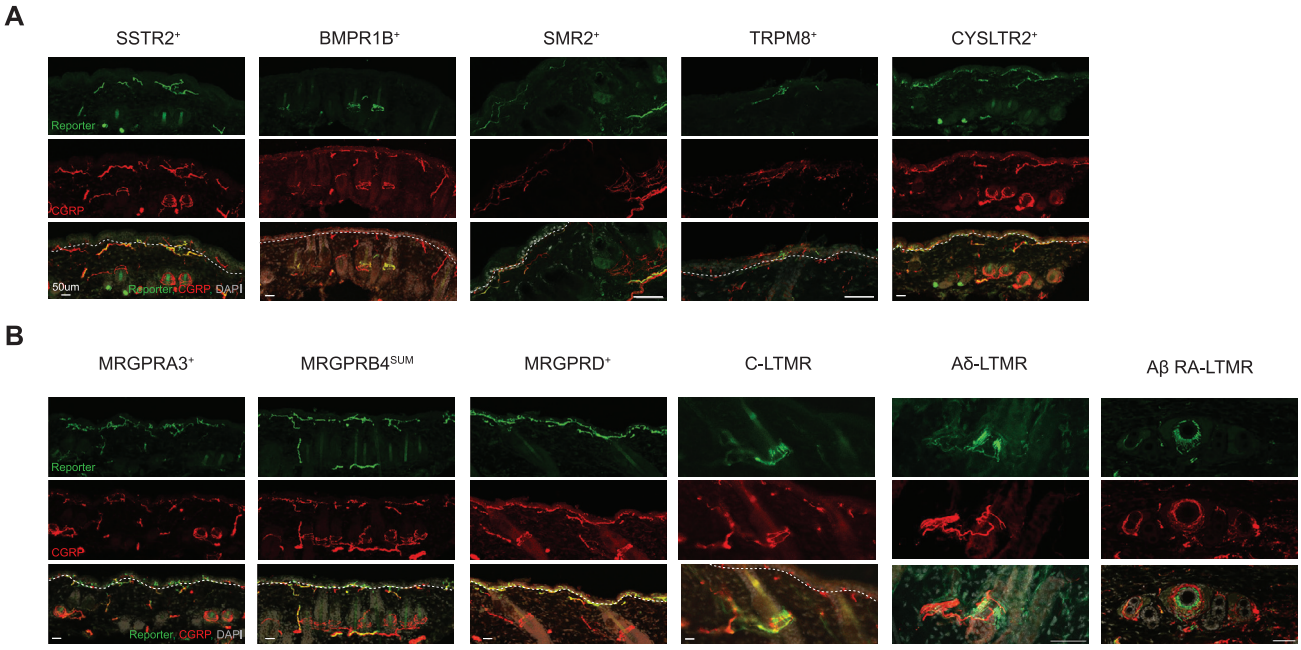

Figure S5. Hairy skin innervation patterns of DRG sensory neuron subtypes, related to Figure 2

(A and B) Representative immunostaining images of hairy skin samples from driver lines generated in this study and existing genetic tools. The panels show the staining of the reporter (GFP or tdTomato) (top), CGRP (middle), and the merge of the two overlaid with DAPI (bottom). The white dashed line indicates the border between the epidermis and dermis. Scale bars, 50 μm.

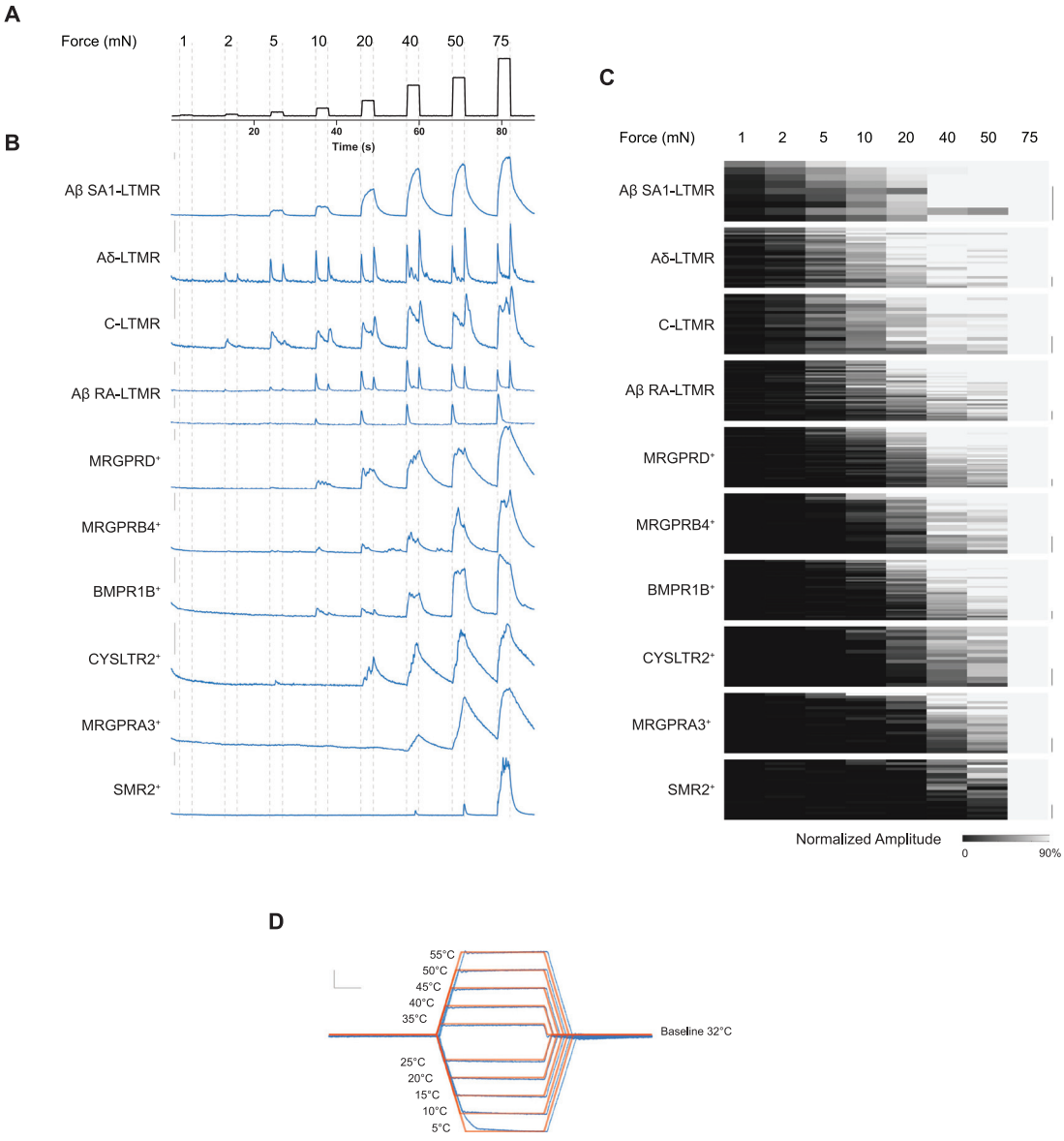

Figure S6. Adaptation properties and stimulus-response relationships of DRG neurons subtypes, related to Figure 4

(A) Prolonged indentation steps, ranging from 1 to 75 mN. The duration of each step indentation for these experiments is 3 s.

(B) Representative response of each DRG neuron subtype aligned to the indentation stimuli. Scale bar is 20% ΔF/F.

(C) Normalized amplitudes of individual neurons from each DRG neuron subtype in response to skin indentation (duration 0.5 s). Each row represents a neuron. The amplitude of calcium response is normalized to the response at 75 mN. The vertical scale refers to five cells.

(D) Temperature stimuli used for the polymodality assay. Red lines refer to the command temperature, and blue lines represent the recorded temperature between the Peltier device and skin. The temperature steps are applied in the following order: 35°C, 25°C, 20°C, 40°C, 15°C, 45°C, 10°C, 50°C, 5°C, and 55°C. The rate of temperature change was kept at 5°C s^{-1}. Scale bars are 5°C (y axis) and 5 s (x axis).

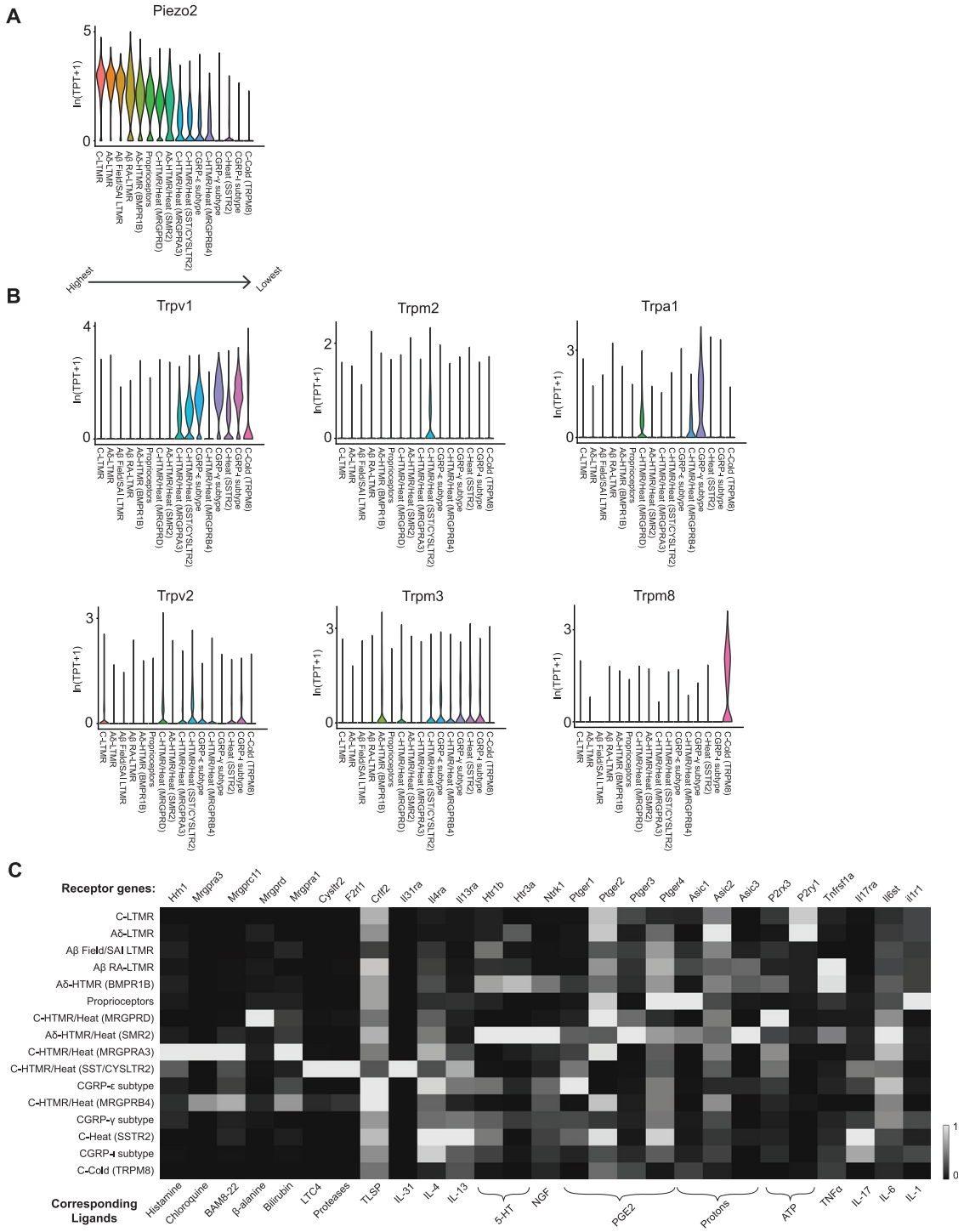

Figure S7. Expression profiles of Piezo2, thermo-TRP channels, and receptors related to itch and pain across DRG neuron subtypes, related to Figure 7

(A) Violin plots displaying the expression profile of Piezo channels. The DRG subtypes are sorted based on their relative level of expression of Piezo2 (highest left, lowest right).

(B) Expression levels of the thermosensitive TRP channels that exhibit detectable levels of expression in one or more DRG neuron subtypes. TPT, tags per ten thousand.

(C) Normalized expression levels genes implicated as receptors for pruritogens and inflammatory mediators of pain across DRG neuron subtypes. The expression levels are normalized to the maximum average expression level for a given receptor. Only genes with detectable expression are shown. LTC4, leukotriene C4; NGF, nerve growth factor; PGE2, prostaglandin E2; TNF-α, tumor necrosis factor alpha.